

Search for features in the spectrum of primordial perturbations using Planck and other datasets

Paul Hunt^a & Subir Sarkar^{b,c}

^aTheoretical Physics, Ludwig Maxmillians University, Theresienstrasse 37, 80333 Munich, Germany

^bRudolf Peierls Centre for Theoretical Physics, University of Oxford, 1 Keble Road, Oxford OX1 3NP, UK

^cNiels Bohr International Academy, Copenhagen University, Blegdamsvej 17, 2100 Copenhagen Ø, Denmark

E-mail: Paul.Hunt@lmu.de, s.sarkar@physics.ox.ac.uk

Abstract. We reconstruct the power spectrum of primordial curvature perturbations by applying a well-validated non-parametric technique employing Tikhonov regularisation to the first data release from the Planck satellite, as well as data from the ground-based ACT and SPT experiments, the WiggleZ galaxy redshift survey, the CFHTLenS tomographic weak lensing survey, and spectral analysis of the ‘Lyman- α forest’. Inclusion of the additional data sets improves the reconstruction on small spatial scales. The reconstructed scalar spectrum (assuming the standard Λ CDM cosmology) is not scale-free but has an infrared cutoff at $k \lesssim 5 \times 10^{-4} \text{ Mpc}^{-1}$ and several $\sim 2 - 3\sigma$ features, of which two at wavenumber $k/\text{Mpc}^{-1} \sim 0.0018$ and 0.057 had been seen already in WMAP data. A higher significance $\sim 4\sigma$ feature at $k \sim 0.12 \text{ Mpc}^{-1}$ is indicated by Planck data, but may be sensitive to the systematic uncertainty around multipole $\ell \sim 1800$ in the 217×217 GHz cross-spectrum. In any case accounting for the ‘look elsewhere’ effect drops its global significance to $\sim 2\sigma$. Adding the preliminary detection of a primordial B-mode polarisation signal by BICEP2 allows reconstruction of the tensor power spectrum as well, however its spectral index has a slope *opposite* to that expected from slow-roll inflation, thus further implicating its likely origin as Galactic dust emission.

Keywords: cosmic microwave background, cosmological parameters, cosmology: large-scale structure of universe, inflation, gravitational waves primordial curvature perturbation

1 Introduction

Detailed knowledge of the primordial curvature perturbation is essential in order to elucidate the physical mechanism which generated it. This is widely believed to be an early quasi-de Sitter phase of exponentially fast expansion (inflation), usually assumed to be driven by a scalar field whose ‘slow-roll’ to the minimum of its potential generates a close to power-law spectrum of curvature perturbations (with small logarithmic corrections called ‘running’).

A power-law spectrum is usually *assumed* when extracting cosmological parameters from observations of the cosmic microwave background (CMB) and large-scale structure (LSS) in the universe. The actual primordial power spectrum (PPS) cannot in fact be directly extracted from the data. This is because relevant cosmological observables are given by a convolution of the primordial perturbations with a smoothing kernel which depends on both the assumed world model and the assumed matter content of the universe. Moreover the deconvolution problem is ill-conditioned so a regularisation scheme must be employed to control error propagation.

We have demonstrated [1] that ‘Tikhonov regularisation’ can reconstruct the primordial spectrum from multiple cosmological data sets and provide reliable estimates of both its uncertainty and resolution. Using Monte Carlo simulations we investigated several methods for selecting the regularisation parameter and found that generalised cross-validation and Mallows’s C_p method give optimal results. We applied our inversion procedure to data from the Wilkinson Microwave Anisotropy Probe (WMAP), other ground-based small angular scale CMB experiments, and the Sloan Digital Sky Survey (SDSS). The reconstructed spectrum (assuming the standard Λ CDM cosmology) was found to have an infrared cutoff at $k \lesssim 5 \times 10^{-4} \text{ Mpc}^{-1}$ (due to the anomalously low CMB quadrupole) and several features with $\sim 2\sigma$ significance at $k/\text{Mpc}^{-1} \sim 0.0013\text{--}0.0023$, $0.036\text{--}0.040$ and $0.051\text{--}0.056$, reflecting the ‘WMAP glitches’ [1]. We noted that more accurate data, such as from the Planck satellite, would be required to test whether these features are indeed real. The issue has become particularly relevant because the recent detection of B-mode polarisation in the CMB by the Background Imaging of Cosmic Extragalactic Polarization (BICEP2) experiment has been attributed to gravitational waves — the ‘smoking gun’ of primordial inflation [24].

In this paper we apply our method to the first data release from the Planck satellite [2], and ground-based experiments such as Atacama Cosmology Telescope (ACT) [3], South Pole Telescope (SPT) [4] and BICEP2/Keck Array [5], as well as the WiggleZ galaxy redshift survey [6] and analysis of the Canada-France Hawaii Telescope Lensing Survey (CFHTLenS) [7] and spectral analysis of the Lyman- α ‘forest’ [8]. Note that the Planck collaboration has estimated cosmological parameters from their data by *assuming* a power-law primordial spectrum, with possible running included [9]. Several authors have adopted a more general parameterisation of the PPS and used Monte Carlo Markov Chain (MCMC) analysis to estimate the PPS and the background cosmological parameters *simultaneously*. However the relatively low number of parameters means that the resolution of the estimated PPS is limited. Up to 4 tilted wavenumber bins with variable locations were used in [10], while [11] employed up to 5 movable knots with linear and cubic spline interpolation and assessed the Bayesian evidence for each additional knot. The Planck team applied a similar procedure to their second data release for up to 8 movable knots with linear interpolation [12]. A cubic spline PPS with 20 fixed knots was applied in analysis of the Planck, ACT, SPT and BOSS CMASS data in [13], while the same method was implemented with 12 fixed knots by the Planck team for the second data release [12]. The PPS has also been modelled by a 12 fixed

knot cubic Hermite polynomial and estimated from CMB and WiggleZ data, together with measurements of σ_8 from CFHTLenS and the Planck Sunyaev-Zeldovich catalogue [14]. In [15] the Planck data and the BICEP2 likelihood function for the tensor-to-scalar ratio r were combined to constrain a linear spline PPS with 1 movable knot. The scalar and tensor power spectra have also been estimated from the Planck and BICEP2 data using a 3 fixed knot cubic spline for either the scalar or tensor spectrum [16].

There have been far fewer *non*-parametric approaches. The Planck team have most recently used a penalised likelihood inversion method involving a B-spline for the PPS [12]; a similar scheme with a 485 knot cubic spline had been used earlier for their first data release [17]. Another example is the inversion of Planck data with Richardson-Lucy deconvolution [18]. An attractive method called PRISM which uses a ‘sparsity’ prior on features in the PPS in a wavelet basis to regularise the inverse problem was developed in [19] and has been subsequently applied to Planck data [20].

In the alternative approach we follow here the background parameters are held fixed, which permits the deconvolution of the smoothing kernel relating the observables to the PPS in linear cosmological perturbation theory. In addition to recovering the scalar PPS alone, we present the first *model-independent* joint reconstruction of the scalar and tensor power spectra.¹ We have refined our earlier method and now use the logarithm of the power spectra in the reconstruction. This ensures that the recovered spectra are positive, and allows us to set priors on the slope of the spectra and impose the ‘inflation consistency relation’ $n_t = -r/8$ for single-field slow-roll models [21]. Moreover we correct for gravitational lensing of the CMB which is important on the small scales probed by the latest experiments.

We confirm that all the features we identified previously [1] in WMAP data are also present in the Planck data at $\gtrsim 2\sigma$ confidence. Moreover there is a new feature at $k/\text{Mpc}^{-1} \sim 0.12\text{--}0.15$ at 4σ confidence, even *after* we take out the 217x217 GHz data from Planck. We did so following the suggestion [22] that there are residual systematics in this particular channel, which was confirmed by the Planck collaboration in their updated paper [9]. This both illustrates the problems in reliably identifying features, but it also makes more compelling the need for further detailed studies. Reliable detection of even *one* feature in the spectrum would immediately rule out *all* slow-roll models of inflation. Hence this is a key probe of inflation, complementary to searches for non-gaussianity and gravitational waves [23].

2 Inversion method

2.1 Tikhonov regularisation

Let us assume there are N available cosmological data sets, each with $N_{\mathbb{Z}}$ data points $d_a^{(\mathbb{Z})}$, from which we wish to estimate the PPS. Here the subscript runs from 1 to $N_{\mathbb{Z}}$ and the superscript \mathbb{Z} denotes the data set. In a flat (or open) universe the points of many data sets are related to the power spectrum $\mathcal{P}_{\mathcal{R}}(k)$ of the curvature perturbation \mathcal{R} by [21]

$$d_a^{(\mathbb{Z})} = \int_0^\infty \mathcal{K}_a^{(\mathbb{Z})}(\boldsymbol{\theta}, k) \mathcal{P}_{\mathcal{R}}(k) dk + n_a^{(\mathbb{Z})}. \quad (2.1)$$

Here the integral kernels $\mathcal{K}_a^{(\mathbb{Z})}$ depend on the background cosmological parameters $\boldsymbol{\theta}$, and the noise vectors $n_a^{(\mathbb{Z})}$ have zero mean and covariance matrices $N_{ab}^{(\mathbb{Z})} \equiv \langle n_a^{(\mathbb{Z})} n_b^{(\mathbb{Z})} \rangle$. In what

¹In previous work either the scalar spectrum [16] or the tensor spectrum [12, 15] was *assumed* to be a power-law.

follows we also include in $\boldsymbol{\theta}$ extraneous ‘nuisance’ parameters associated with the likelihood functions of the data sets, such as calibration parameters or the parameters describing the CMB foregrounds. We assume an estimate $\hat{\boldsymbol{\theta}}$ of the background and nuisance parameters exists which is *independent* of the N data sets, and has a zero mean uncertainty \mathbf{u} , with elements u_α . Then $\langle u_\alpha n_a^{(\mathbb{Z})} \rangle = 0$ for all elements of the uncertainty and noise vectors as these are uncorrelated by assumption. The covariance matrix for the estimated background parameters is just $\mathbf{U} \equiv \langle \mathbf{u} \mathbf{u}^T \rangle$, where T signifies the matrix transpose. Given our estimate of the background and nuisance parameter set $\hat{\boldsymbol{\theta}}$, the goal is to obtain an estimate $\hat{\mathcal{P}}_{\mathcal{R}}(k)$ of the PPS from the data sets.

The PPS is approximated as a piecewise function given by a sum of N_j basis functions $\phi_i(k)$, weighted by coefficients p_i :

$$\mathcal{P}_{\mathcal{R}}(k) = \sum_{i=1}^{N_j} p_i \phi_i(k). \quad (2.2)$$

For a grid of wavenumbers $\{k_i\}$ the basis functions are defined as

$$\phi_i(k) \equiv \begin{cases} 1, & k_i < k \leq k_{i+1}, \\ 0, & \text{elsewhere.} \end{cases} \quad (2.3)$$

We use a logarithmically spaced grid between $k_1 = 7 \times 10^{-6} \text{ Mpc}^{-1}$ and $k_{N_j+1} = 30 \text{ Mpc}^{-1}$ with $N_j = 2500$. Substituting Eq.(2.2) into Eq.(2.1) gives

$$\mathbf{d}_a^{(\mathbb{Z})} = \sum_i W_{ai}^{(\mathbb{Z})}(\boldsymbol{\theta}) p_i + \mathbf{n}_a^{(\mathbb{Z})}, \quad (2.4)$$

where the $N_{\mathbb{Z}} \times N_j$ matrices $W_{ai}^{(\mathbb{Z})}(\boldsymbol{\theta})$ depend on the background parameters:

$$W_{ai}^{(\mathbb{Z})}(\boldsymbol{\theta}) = \int_{k_i}^{k_{i+1}} \mathcal{K}_a^{(\mathbb{Z})}(\boldsymbol{\theta}, k) dk. \quad (2.5)$$

As discussed in [1] solving Eq.(2.1) for the PPS is an ill-posed inverse problem and the matrices $W_{ai}^{(\mathbb{Z})}$ are ill-conditioned. Consequently naïve attempts to determine the PPS by maximising the likelihood function $\mathcal{L}(\mathbf{p}, \boldsymbol{\theta} | \mathbf{d})$ of the data \mathbf{d} given \mathbf{p} and $\boldsymbol{\theta}$ produce ill-behaved spectra with wild irregular oscillations. To overcome this, Tikhonov regularisation uses a penalty function $R(\mathbf{p})$ which takes on large values for unphysical spectra. Then the likelihood is maximised subject to the constraint that the penalty function at most equals a certain value R_0 ,

$$\max_{\mathbf{p}} \mathcal{L}(\mathbf{p}, \boldsymbol{\theta} | \mathbf{d}) \quad \text{subject to} \quad R(\mathbf{p}) \leq R_0. \quad (2.6)$$

Rather than working directly with \mathbf{p} we use instead \mathbf{y} with elements $y_i = \ln p_i$ in order to enforce the positivity constraint on the recovered PPS. Thus the estimated PPS is given by

$$\hat{\mathbf{y}}(\mathbf{d}, \hat{\boldsymbol{\theta}}, \lambda) = \min_{\mathbf{y}} Q(\mathbf{y}, \mathbf{d}, \hat{\boldsymbol{\theta}}, \lambda), \quad (2.7)$$

where

$$Q(\mathbf{y}, \mathbf{d}, \hat{\boldsymbol{\theta}}, \lambda) \equiv L(\mathbf{y}, \hat{\boldsymbol{\theta}}, \mathbf{d}) + \lambda R(\mathbf{y}). \quad (2.8)$$

Here $L(\mathbf{p}, \boldsymbol{\theta}, \mathbf{d}) \equiv -2 \ln \mathcal{L}(\mathbf{p}, \boldsymbol{\theta} | \mathbf{d})$ and the regularisation parameter λ plays the role of a Lagrange multiplier.

Since to a first approximation the PPS is a power-law with a constant spectral index $n_s - 1 = d \ln \mathcal{P}_{\mathcal{R}} / d \ln k$ we use the penalty function

$$R_s(\mathbf{y}) = \sum_{i=1}^{N_k-1} [y_{i+1} - y_i - (n_s - 1) \Delta \ln k]^2, \quad (2.9)$$

$$\propto \int \left(\frac{d \ln \mathcal{P}_{\mathcal{R}}}{d \ln k} - n_s + 1 \right)^2 d \ln k, \quad (2.10)$$

where $\Delta \ln k$ is the logarithmic separation of the $\{k_i\}$ wavenumber grid. Using the $(N_k - 1) \times N_k$ first difference matrix \mathbf{L} and the $N_k \times N_k$ matrix Γ given by

$$\mathbf{L} = \begin{pmatrix} -1 & 1 & & & \\ & -1 & 1 & & \\ & & \ddots & \ddots & \\ & & & -1 & 1 \\ & & & & -1 & 1 \end{pmatrix}, \quad \Gamma \equiv \mathbf{L}^T \mathbf{L} = \begin{pmatrix} 1 & -1 & & & \\ -1 & 2 & -1 & & \\ & \ddots & \ddots & \ddots & \\ & & -1 & 2 & -1 \\ & & & -1 & 1 \end{pmatrix}, \quad (2.11)$$

together with the $N_k - 1$ vector $\boldsymbol{\eta}$ with elements $\eta_i \equiv (n_s - 1) \Delta \ln k$ the penalty function can be written as

$$R_s(\mathbf{y}) = \mathbf{y}^T \Gamma \mathbf{y} - 2 \boldsymbol{\eta}^T \mathbf{L} \mathbf{y} + \boldsymbol{\eta}^T \boldsymbol{\eta}. \quad (2.12)$$

It penalises large excursions and conservatively smooths the estimated PPS towards a power-law of amplitude set by the data and a ‘prior’ spectral index n_s . The pseudo Newton-Raphson algorithm of [1] is again employed to minimise Q and estimate the PPS.

It is straightforward to extend our method to include the reconstruction of the tensor PPS $\mathcal{P}_h(k)$, where h_{ij} is the tensor perturbation [21]. For simplicity the same basis functions with the same wavenumber grid are used for the tensor PPS as for the scalar PPS so that

$$\mathcal{P}_h(k) = \sum_{i=1}^{N_j} \mathbf{q}_i \phi_i(k). \quad (2.13)$$

We introduce \mathbf{z} with elements $z_i = \ln q_i$ and define the vectors $\mathbf{P} \equiv (\mathbf{p}^T, \mathbf{q}^T)^T$ and $\mathbf{Y} \equiv (\mathbf{y}^T, \mathbf{z}^T)^T$ with length $2N_k$. The tensor penalty function is

$$R_t(\mathbf{z}) = \mathbf{z}^T \Gamma \mathbf{z} - 2 \boldsymbol{\mu}^T \mathbf{L} \mathbf{z} + \boldsymbol{\mu}^T \boldsymbol{\mu}, \quad (2.14)$$

where the vector $\boldsymbol{\mu}$ has elements $\mu_i = n_t \Delta \ln k$ as the tensor spectral index is conventionally $n_t = d \ln \mathcal{P}_h / d \ln k$. The joint estimate of the scalar and tensor power spectra is then

$$\hat{\mathbf{Y}}(\mathbf{d}, \hat{\boldsymbol{\theta}}, \lambda) = \min_{\mathbf{Y}} Q(\mathbf{Y}, \mathbf{d}, \hat{\boldsymbol{\theta}}, \lambda), \quad (2.15)$$

where

$$Q(\mathbf{Y}, \mathbf{d}, \hat{\boldsymbol{\theta}}, \lambda) \equiv L(\mathbf{Y}, \hat{\boldsymbol{\theta}}, \mathbf{d}) + \lambda [R_s(\mathbf{y}) + c_{\text{dust}} R_t(\mathbf{z})]. \quad (2.16)$$

As explained in § 3.4 the constant c_{dust} ensures that the recovered tensor spectrum is not over smoothed as the BICEP2/Keck Array dust power increases. Note that here we have used the *same* regularisation parameter for both the scalar and tensor penalty functions, but this can easily be changed as necessary.

2.2 CMB lensing

After last scattering CMB photons are gravitationally deflected by large scale structure. This CMB lensing smooths the acoustic peaks of the temperature and polarisation angular power spectra, and also generates B-mode polarisation on small scales. ACT, SPT and Planck have all detected CMB lensing at high significance assuming a power-law PPS [25–27]. Since lensing changes the TT spectrum by around 20% at $\ell = 3000$ it *must* be taken into account in order to obtain an accurate PPS reconstruction.

The deflection angle equals the gradient of the lensing potential ψ , which is given by a weighted integral of the gravitational potential along the line of sight. The power spectrum of the lensing potential $s_\ell^\psi = \ell(\ell+1)C_\ell^\psi/2\pi$ can be written as [28]

$$s_\ell^\psi = \int_0^\infty \mathcal{K}_\ell^\psi(\boldsymbol{\theta}, k) \mathcal{P}_\mathcal{R}(k) dk. \quad (2.17)$$

We include the effects of nonlinear structure formation in the kernel \mathcal{K}_ℓ^ψ as calculated by the **Halofit** [57] fitting formula for the nonlinear matter power spectrum in the same way as [29], but applied with a fixed fiducial PPS. Substituting Eq.(2.2) into the above equation gives $s_\ell^\psi = \sum_i W_{\ell i}^\psi p_i$. Two quantities which characterise the statistical properties of the deflection angle are

$$\sigma^2(r) = \sum_\ell \frac{\ell^2}{\ell+1} [1 - J_0(\ell r)] s_\ell^\psi, \quad (2.18)$$

$$C_{\text{gl},2}(r) = \sum_\ell \frac{\ell^2}{\ell+1} J_2(\ell r) s_\ell^\psi, \quad (2.19)$$

where J_0 and J_2 are Bessel functions.

The predicted CMB angular power spectra $\ell(\ell+1)C_\ell^I/2\pi$ where $I \in \{\text{TT}, \text{TE}, \text{EE}, \text{BB}\}$ are denoted s_ℓ^I . The unlensed scalar and tensor temperature power spectra are $s_{\ell,s}^{\text{TT}} = \sum_i W_{\ell i,s}^{\text{TT}} p_i$ and $s_{\ell,t}^{\text{TT}} = \sum_i W_{\ell i,t}^{\text{TT}} q_i$ respectively, where the scalar and tensor matrices $W_{\ell i,s}^{\text{TT}}$ and $W_{\ell i,t}^{\text{TT}}$ are calculated from the scalar and tensor temperature integral kernels as in Eq.(2.5). In the Boltzmann code **CAMB** used for this work the total lensed temperature power spectrum is² $s_\ell^{\text{TT}} = \tilde{s}_{\ell,s}^{\text{TT}} + s_{\ell,t}^{\text{TT}}$. Here the lensed scalar TT spectrum $\tilde{s}_{\ell,s}^{\text{TT}}$ is related to the unlensed spectrum by $\tilde{s}_{\ell,s}^{\text{TT}} = \sum_{\ell'} \mathcal{W}_{\ell\ell'}^{\text{TT}} s_{\ell',s}^{\text{TT}}$ in the perturbative ‘flat-sky’ approximation of [30, 31], where

$$\mathcal{W}_{\ell\ell'}^{\text{TT}} = \frac{\ell(\ell+1)}{\ell'+1} \int_0^\pi e^{-\ell'^2 \sigma^2(r)/2} J_0(\ell r) \left[J_0(\ell' r) + \frac{\ell'^2}{2} C_{\text{gl},2}(r) J_2(\ell' r) \right] r dr. \quad (2.20)$$

To obtain $\hat{\mathbf{y}}$ by minimising Q we need the derivative

$$\frac{\partial L_{\text{CMB}}}{\partial y_i} = \sum_{\ell\ell'} \frac{\partial L_{\text{CMB}}}{\partial s_\ell^{\text{TT}}} \left(\mathcal{W}_{\ell\ell'}^{\text{TT}} W_{\ell' i,s}^{\text{TT}} + \sum_{\ell''} \frac{\partial \mathcal{W}_{\ell\ell'}^{\text{TT}}}{\partial s_{\ell''}^\psi} s_{\ell'',s}^{\text{TT}} W_{\ell' i}^\psi \right) p_i. \quad (2.21)$$

Here L_{CMB} is the sum of the ACT, SPT and Planck likelihood functions, and

$$\begin{aligned} \frac{\partial \mathcal{W}_{\ell\ell'}^{\text{TT}}}{\partial s_{\ell''}^\psi} &= \frac{\ell(\ell+1)\ell'^2\ell''^2}{2(\ell'+1)(\ell''+1)} \int_0^\pi e^{-\ell'^2 \sigma^2(r)/2} J_0(\ell r) \left\{ J_2(\ell'' r) J_0(\ell' r) \right. \\ &\quad \left. - [1 - J_0(\ell'' r)] \left[J_0(\ell' r) + \frac{\ell'^2}{2} C_{\text{gl},2}(r) J_2(\ell' r) \right] \right\} r dr. \end{aligned} \quad (2.22)$$

²Tensor lensing is not implemented in **CAMB** as it has a negligible effect.

The derivative $\partial L_{\text{CMB}}/\partial s_{\ell}^{\text{TT}}$ is a function of $\tilde{s}_{\ell,s}^{\text{TT}}$, which is calculated from $s_{\ell,s}^{\text{TT}}$ at each iteration of the Newton-Raphson minimisation algorithm using the more accurate but complicated curved-sky correlation function method of [29] as implemented in CAMB. The effect of the lensing correction is shown in Fig. 1. Since lensing smooths the acoustic peaks, neglecting it means that fitting the data requires spurious oscillatory features in the recovered PPS on small scales. Including the lensing correction *removes* these spurious features.

Lensing of the EE and TE spectra is neglected as it has a negligible effect for the data sets considered here. Thus $s_{\ell}^{\text{EE}} = s_{\ell,s}^{\text{EE}} + s_{\ell,t}^{\text{EE}}$ where $s_{\ell,s}^{\text{EE}} = \sum_i W_{\ell i,s}^{\text{EE}} p_i$ and $s_{\ell,t}^{\text{EE}} = \sum_i W_{\ell i,t}^{\text{EE}} q_i$, and similarly for the TE spectrum. The total BB spectrum is given by $s_{\ell}^{\text{BB}} = \tilde{s}_{\ell,s}^{\text{BB}} + s_{\ell,t}^{\text{BB}}$ where $s_{\ell,t}^{\text{BB}} = \sum_i W_{\ell i,t}^{\text{BB}} q_i$ is the contribution from primordial tensor perturbations and $\tilde{s}_{\ell,s}^{\text{BB}} = \sum_{\ell'} W_{\ell\ell'}^{\text{BB}} s_{\ell',s}^{\text{EE}}$ results from the conversion of E-mode polarisation into B-mode by lensing. Here

$$\mathcal{W}_{\ell\ell'}^{\text{BB}} = \frac{\ell(\ell+1)}{\ell'+1} \int_0^{\pi} e^{-\ell'^2 \sigma^2(r)/2} \left\{ J_0(\ell r) \left[J_0(\ell' r) + \frac{\ell'^2}{2} C_{\text{gl},2}(r) J_2(\ell' r) \right] - J_4(\ell r) \left[J_4(\ell' r) + \frac{\ell'^2}{4} C_{\text{gl},2}(r) J_2(\ell' r) + \frac{\ell'^2}{4} C_{\text{gl},2}(r) J_6(\ell' r) \right] \right\} r dr, \quad (2.23)$$

in the flat-sky approximation. The BICEP2/Keck Array likelihood function in Eq.(A.41) involves the EE and BB bandpowers s_b^{EE} (A.44) and s_b^{BB} (A.45) constructed using the window function matrices $W_{b\ell}^{\text{EE}}$ and $W_{b\ell}^{\text{BB}}$ respectively. Therefore the derivative of the likelihood is

$$\begin{aligned} \frac{\partial L_{\text{BICEP}}}{\partial y_i} &= \sum_{b\ell} \left[\frac{\partial L_{\text{BICEP}}}{\partial s_b^{\text{EE}}} W_{b\ell}^{\text{EE}} W_{\ell i,s}^{\text{EE}} \right. \\ &\quad \left. + \frac{\partial L_{\text{BICEP}}}{\partial s_b^{\text{BB}}} \sum_{\ell'} W_{b\ell}^{\text{BB}} \left(\mathcal{W}_{\ell\ell'}^{\text{BB}} W_{\ell' i}^{\text{EE}} + \sum_{\ell''} \frac{\partial \mathcal{W}_{\ell\ell'}^{\text{BB}}}{\partial s_{\ell''}^{\psi}} s_{\ell'',s}^{\text{EE}} W_{\ell' i}^{\psi} \right) \right] p_i. \end{aligned} \quad (2.24)$$

Again $\tilde{s}_{\ell,s}^{\text{BB}}$ is updated at each iteration using the correlation-function method. The derivative $\partial L_{\text{BICEP}}/\partial z_i$ is evaluated similarly.

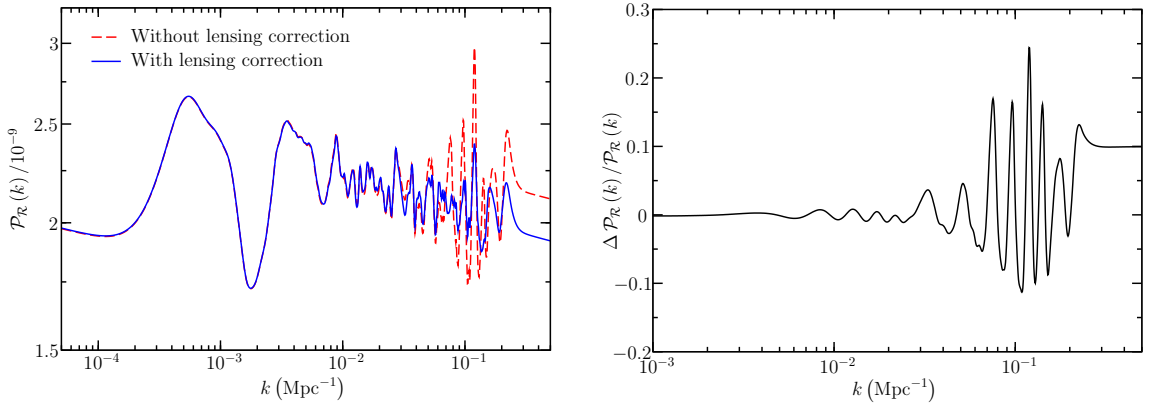


Figure 1. Left: Comparison of the spectra recovered with $\lambda = 400$ from the Planck, WMAP-9 polarisation, ACT and SPT data, with and without correcting for gravitational lensing. Right: The fractional change $[\mathcal{P}_{\mathcal{R}}^{\text{No-Lens}}(k) - \mathcal{P}_{\mathcal{R}}(k)] / \mathcal{P}_{\mathcal{R}}(k)$ in the recovered PPS due to the lensing correction.

3 Results

In [1] following tests using mock data we performed reconstructions with both $\lambda = 100$ and $\lambda = 5000$. We desire comparable results in this paper, but are now working with the *logarithmic* elements $y_i = \ln p_i$ instead of p_i in the inversion. For data sets with Gaussian likelihood functions, $\partial \hat{y}_i / \partial d_a^{(\mathbb{Z})} \propto \left[\sum_{\mathbb{Z}, a, b} p_i W_{ia}^{(\mathbb{Z})} (N^{(\mathbb{Z})})_{ab}^{-1} W_{jb}^{(\mathbb{Z})} p_j + \lambda \Gamma_{ij} \right]^{-1}$ in the logarithm-based reconstruction, whereas $\partial \hat{p}_i / \partial d_a^{(\mathbb{Z})} \propto \left[\sum_{\mathbb{Z}, a, b} W_{ia}^{(\mathbb{Z})} (N^{(\mathbb{Z})})_{ab}^{-1} W_{jb}^{(\mathbb{Z})} + \lambda \Gamma_{ij} \right]^{-1}$ in the non-logarithmic case. As a result the regularisation parameter must be a factor of $p_i^2 \simeq 4$ (in units of 10^{-9}) larger for a logarithmic reconstruction to approximate a non-logarithmic one. Hence we now use $\lambda = 400$ and $\lambda = 20000$. As shown in Appendix B these values provide a close to *optimal* compromise between the resolution and the variance of the reconstruction.

We choose a standard Λ CDM model when performing the reconstructions. The background cosmological and foreground parameter values, which are consistent with those obtained by the Planck team [9] are listed in Table 1.

Parameter type	Parameter	Value	Parameter type	Parameter	Value
Cosmological	$\Omega_b h^2$	0.02240	ACT + SPT	$A_{148}^{\text{PS, ACT}}$	11.93
	$\Omega_c h^2$	0.1145		$A_{218}^{\text{PS, ACT}}$	84.7
	H_0	69.6		$A_{95}^{\text{PS, SPT}}$	8.00
	τ	0.077		$A_{150}^{\text{PS, SPT}}$	10.51
Planck	A_{100}^{PS}	223		$A_{220}^{\text{PS, SPT}}$	84.3
	A_{143}^{PS}	76		$r_{95 \times 150}^{\text{PS}}$	0.924
	A_{217}^{PS}	61		$r_{95 \times 220}^{\text{PS}}$	0.751
	A_{143}^{CIB}	3.40		$r_{150 \times 220}^{\text{PS}}$	0.926
	A_{217}^{CIB}	50		$A_{\text{dust}}^{\text{ACTs}}$	0.40
	A_{143}^{tSZ}	4.99		$A_{\text{dust}}^{\text{ACTe}}$	0.80
	$r_{143 \times 217}^{\text{PS}}$	0.849		y_{148}^{ACTs}	0.9913
	$r_{143 \times 217}^{\text{CIB}}$	1.000		y_{218}^{ACTs}	1.002
	γ^{CIB}	0.548		y_{148}^{ACTe}	0.9873
	c_{100}	1.00068		y_{218}^{ACTe}	0.961
	c_{217}	1.00005		y_{95}^{SPT}	0.9848
	$\xi^{\text{tSZ} \times \text{CIB}}$	0.000		y_{150}^{SPT}	0.9845
	A_{143}^{tSZ}	4.99		y_{220}^{SPT}	1.0173
	A^{kSZ}	0.717	WiggleZ	b	1.00069
	$\beta_1^{100 \times 100}$	0.710	Lyman- α	A	0.545

Table 1. Parameter values used when performing the reconstructions. The cosmological parameters were obtained by a fit to data combination IV, assuming a power-law spectrum.

The inversion method is applied to the following 5 combinations of data sets:

- Data combination I: Planck + WMAP-9 polarisation
- Data combination II: Combination I + ACT + SPT
- Data combination III: Combination II + WiggleZ + galaxy clusters
- Data combination IV: Combination III + CFHTLenS weak lensing + VHS Lyman- α data
- Data combination V: Combination III + BICEP2/Keck Array

The scalar spectrum is recovered from combinations I–IV, while the scalar and tensor spectra are recovered jointly from combination V. The data sets and their likelihood functions are discussed in Appendix A. Throughout we use a prior of $n_s = 0.969$ in the scalar penalty function (2.12), corresponding to the best-fit power-law PPS to data combination IV.

The scalar PPS found from the Planck and WMAP-9 polarisation data exhibits a number of interesting deviations from a power-law, as shown in Figs. 2 and 3. For $k \lesssim 0.03 \text{ Mpc}^{-1}$ the PPS is similar to that recovered from the WMAP-9 temperature angular power spectrum in [1]. As in the earlier reconstruction, there is a cutoff on large scales from the low TT quadrupole followed by dips at $k \simeq 0.0018$, 0.0070 and 0.013 Mpc^{-1} due to a deficit in power around the $\ell \simeq 22$, 90 and 180 multipoles of the Planck TT spectrum, and peaks at $k \simeq 0.0034$ and 0.0088 Mpc^{-1} due to the excess power around the $\ell \simeq 40$ and 120 multipoles. A peak at $k \simeq 0.027 \text{ Mpc}^{-1}$ and dips at $k \simeq 0.032$ and 0.039 Mpc^{-1} correspond to the excess around $\ell \simeq 370$ and the deficits around $\ell \simeq 410$ and 540 respectively. A deficit around $\ell \simeq 800$ causes a dip at $k \simeq 0.057 \text{ Mpc}^{-1}$. Peaks at $k \simeq 0.10$ and 0.12 Mpc^{-1} and a dip at $k \simeq 0.105 \text{ Mpc}^{-1}$ originate from the excesses around $\ell \simeq 1350$ and 1600 and the deficit around $\ell \simeq 1450$ respectively. We *exclude* the $217 \times 217 \text{ GHz}$ cross-spectrum for $1700 < \ell < 1860$ because these multipoles are known to be contaminated by electromagnetic interference from the 4K Joule-Thomson cryogenic cooler, as discussed in Appendix A.1. Hence the dip at $k \simeq 0.14 \text{ Mpc}^{-1}$ arises from the deficit around $\ell \simeq 1800$ in the $143 \times 217 \text{ GHz}$ cross-spectrum alone and is presumably uncontaminated.

Adding the ACT and SPT observations improves the reconstruction over the range $0.08 \lesssim k \lesssim 0.28 \text{ Mpc}^{-1}$. A deficit around $\ell \simeq 2450$ introduces a dip at $k \simeq 0.19 \text{ Mpc}^{-1}$. Including the WiggleZ and galaxy cluster data, which cover $0.02 \lesssim k \lesssim 0.25 \text{ Mpc}^{-1}$, deepens the dips at $k \simeq 0.032 \text{ Mpc}^{-1}$ and $k \simeq 0.19 \text{ Mpc}^{-1}$. The reconstruction is extended to smaller scales by the weak lensing and Lyman- α measurements, which together span $0.01 \lesssim k \lesssim 2.0 \text{ Mpc}^{-1}$. The spectra in Fig. 3 recovered with $\lambda = 20000$ are suppressed for $k \lesssim 0.003 \text{ Mpc}^{-1}$ due to the deficit at $\ell \simeq 22$. The dip at $k \simeq 0.14 \text{ Mpc}^{-1}$ is the most significant.

The predicted Planck, ACT, SPT and WiggleZ data derived from the recovered spectra match the measured data well, as shown in Fig. 4 to Fig. 7. However, the predicted CFHTLenS $\xi_+(\theta)$ shear correlation is systematically *higher* than the data, as seen in Fig. 8. This is consistent with the tension between CFHTLenS and Planck for a power-law PPS that has been reported in the literature, the cause of which is an open question at present [9, 32–35]. Planck is known to favour a slightly higher value of σ_8 than galaxy cluster abundance observations [36, 66]. Here for $\lambda = 500$ the galaxy cluster parameter is $\Sigma_8 \equiv \sigma_8 (\Omega_m/0.27)^{0.3} = 0.809$, while $\Sigma_8 = 0.808$ for $\lambda = 20000$. This is higher than, but not inconsistent with, the value $\Sigma_8 = 0.797 \pm 0.05$ obtained by the cluster abundance observations listed in Appendix A.5.

The VHS Lyman- α data is consistent with the CMB, WiggleZ and galaxy cluster data for a calibration parameter $A = 0.54$, a 1.9σ deviation from the expected value of unity. This is in agreement with [37] which found that the VHS data for $A = 1$ is approximately a factor of 2 higher than expected from the WMAP-3 results.

The large-scale cutoff, $k \simeq 0.0018 \text{ Mpc}^{-1}$ dip and $k \simeq 0.0034 \text{ Mpc}^{-1}$ peak have been observed in model-independent PPS estimates since the release of the WMAP-1 data [23]. Our data combination I reconstruction with $\lambda = 400$ is clearly consistent with the PPS found from the $50 \leq \ell \leq 2500$ data by the Planck team using their penalised likelihood method [17]. Similar features can be seen at e.g. $k \simeq 0.027$, 0.057 , 0.12 and 0.14 Mpc^{-1} . The latter three fluctuations were also emphasised in the Richardson-Lucy deconvolution study [18].

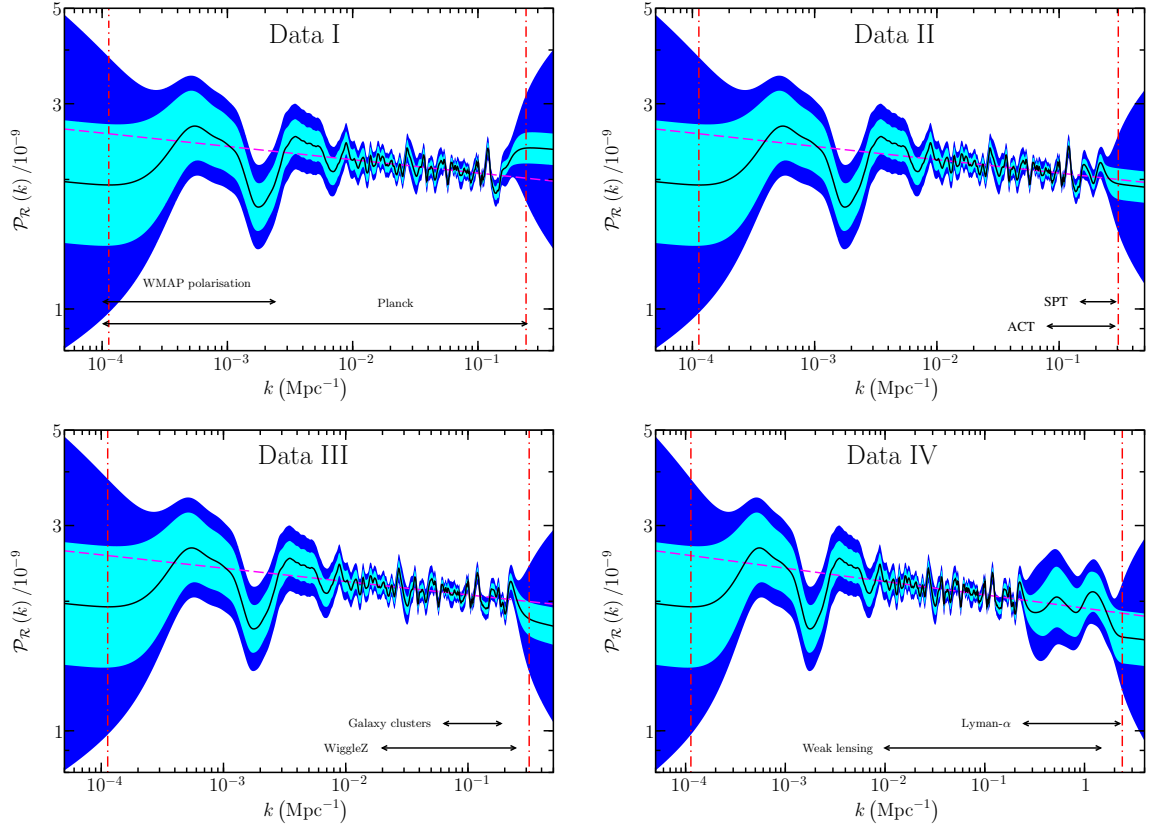


Figure 2. Primordial power spectra recovered from data combinations I to IV involving the Planck, WMAP-9 polarisation, ACT, SPT, WiggleZ, galaxy clustering, CFTHLenS and Lyman- α data, with $\lambda = 400$, compared to the ‘best-fit’ power-law spectrum (slope $n_s = 0.969$, magenta dashed line). In all panels the central black line is the reconstruction adopting this n_s value as a prior, and the dark band is the 1σ error given by the square root of the diagonal elements of the Bayesian covariance matrix Π (B.21), while the smaller light band is similarly obtained from the frequentist covariance matrix Σ_F (B.19). Vertical lines delineate the wavenumber range covered by the resolution kernels (see Fig.17) over which the reconstruction is faithful to the true PPS, while the horizontal lines indicate the wavenumber range over which specific datasets have most impact.

3.1 Background and nuisance parameter errors

To demonstrate how errors in the background and nuisance parameters affect the recovered PPS, we calculate the covariance matrix Σ_P (B.20) using the error matrix

$$\begin{aligned} \mathbf{U} = \text{diag} & \left[(0.012 \omega_b)^2, (0.022 \omega_c)^2, (0.018 h)^2, (0.15 \tau)^2, (0.030 b)^2, (0.53 A)^2, \right. \\ & \left(0.061 A_{220}^{\text{PS, SPT}}\right)^2, (0.026 r_{150 \times 220}^{\text{PS}})^2, (0.20 r_{95 \times 220}^{\text{PS}})^2, (0.11 r_{95 \times 150}^{\text{PS}})^2, \left(0.056 A_{148}^{\text{PS, ACT}}\right)^2, \\ & (0.24 A_{100}^{\text{PS}})^2, (0.089 r_{143 \times 217}^{\text{PS}})^2, \left(0.060 A_{218}^{\text{PS, ACT}}\right)^2, \left(0.051 A_{150}^{\text{PS, SPT}}\right)^2, (0.10 A_{217}^{\text{CIB}})^2, \\ & \left. (0.59 A_{143}^{\text{tSZ}})^2 \right]. \end{aligned} \quad (3.1)$$

Here some selected nuisance parameters associated with the CMB foregrounds f_ℓ^I defined in Appendix A are included. These errors correspond to the uncertainties in the parameter

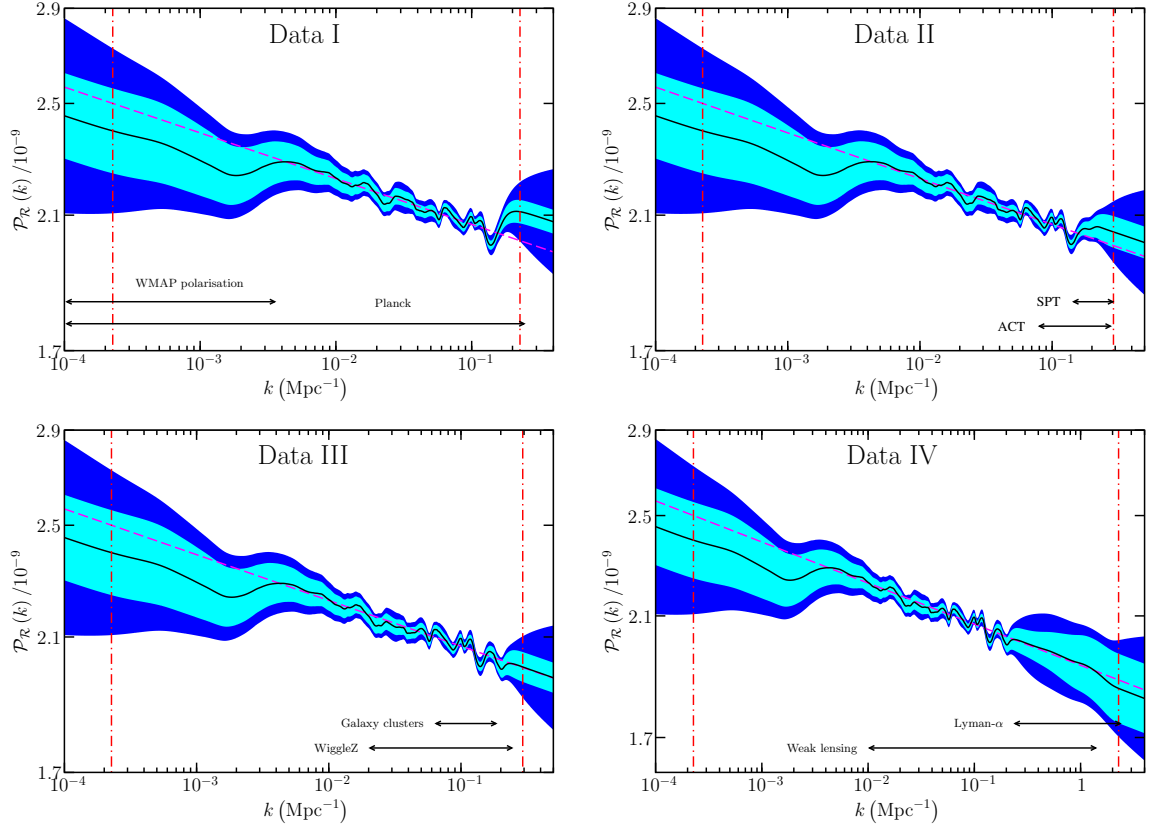


Figure 3. As Fig.2 but for $\lambda = 20000$.

values obtained from the Planck, ACT, SPT and WiggleZ data assuming a power-law PPS.³

The effect of the foreground parameter uncertainties on the diagonal elements of the matrix Σ_P is shown in Fig.9. The contribution of the foregrounds f_ℓ^I to the total TT angular power spectrum increases with the multipole moment ℓ . Hence the error due to uncertainties in the foreground parameters is greatest at $k \simeq 0.25 \text{ Mpc}^{-1}$, which is approximately the smallest scale probed by the CMB data. As discussed in detail in [1], the patterns of peaks on intermediate scales in Fig.10 is due to the effects of uncertainties in the background parameters propagating through the CMB acoustic peaks. The Sachs-Wolfe plateau is more insensitive to the background parameters and so the error is lower on large scales. The error on small scales is dominated by the uncertainty in the Lyman- α calibration parameter A . At $k \simeq 0.25 \text{ Mpc}^{-1}$ the error due to uncertainties in nuisance parameters is comparable with that from background parameter uncertainties. On intermediate and small scales the error due to uncertain background and nuisance parameter values is greater than that due to noise in the data.

3.2 Uncorrelated bandpowers

Our understanding of the recovered PPS is complicated by the correlation between neighbouring PPS elements due to the smoothing criterion. To overcome this we calculate *uncorrelated*

³Although our analysis assumes that the data sets used to estimate the background and nuisance parameters are different from those used to recover the PPS, the parameter error matrix is used merely as an example.

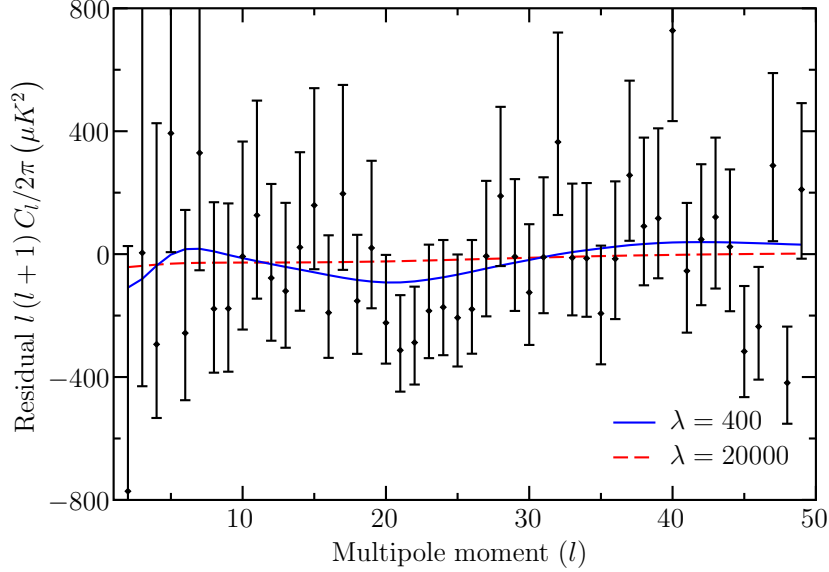


Figure 4. Fits to the $\ell < 50$ Planck TT data (residuals) of primordial power spectra recovered with $\lambda = 400$ (full blue line) and 20000 (dashed red line) from the Planck, WMAP-9 polarisation, ACT, SPT, WiggleZ, galaxy clustering, CFTHLenS and Lyman- α data (combination IV). The residuals are obtained by subtracting off the TT spectrum of the best-fit $n_s = 0.969$ power-law spectrum.

bandpowers which represent the independent degrees of the freedom of the reconstruction using the method of [1]. Correlated bandpowers (with a non-diagonal frequentist covariance matrix Σ_N) are transformed into uncorrelated bandpowers (with a diagonal covariance matrix) by multiplication with a set of window functions. These are the rows of the Hermitian square root of Σ_N^{-1} , normalised to sum to unity. The effective number of free parameters of the reconstruction is estimated by the quantity $\nu_1 \equiv \sum_{\mathbb{Z}, i, a} W_{ai}^{(\mathbb{Z})} M_{ia}^{(\mathbb{Z})}$. Since $\nu_1 = 56.5$ for $\lambda = 400$ and $\nu_1 = 16.85$ for $\lambda = 20000$ we choose 57 bandpowers for $\lambda = 400$ and 17 bandpowers for $\lambda = 20000$. The correlated bandpowers are chosen so that the window functions are as well-behaved and non-negative as possible. Figs.11 and 12 show the window functions and uncorrelated bandpowers. The window functions are lower and less localised at the wavenumbers corresponding to the troughs of the CMB angular power spectrum, where the resolution is reduced.

3.3 Statistical significance of the features

We need to establish if the features in the PPS reconstructions are consistent with noise-induced artifacts or if they represent genuine departures of the true PPS from a power-law. We perform a hypothesis test with the null hypothesis being that the true spectrum is the best-fit power-law to data combination IV, which has $n_s = 0.969$, and invert 10^6 mock data realisations generated using the null hypothesis PPS. The $\ell < 50$ CMB data points were simulated by sampling a Wishart distribution as in [1], while the other data points were drawn from Gaussian distributions with the correct covariance matrices. The distribution of the results is compared to the reconstruction from the real data in Fig.13, which gives a visual indication of the statistical significance of the features in the reconstruction. The mean of the recovered spectra is biased low on large scales with $\lambda = 400$ due to the non-Gaussian

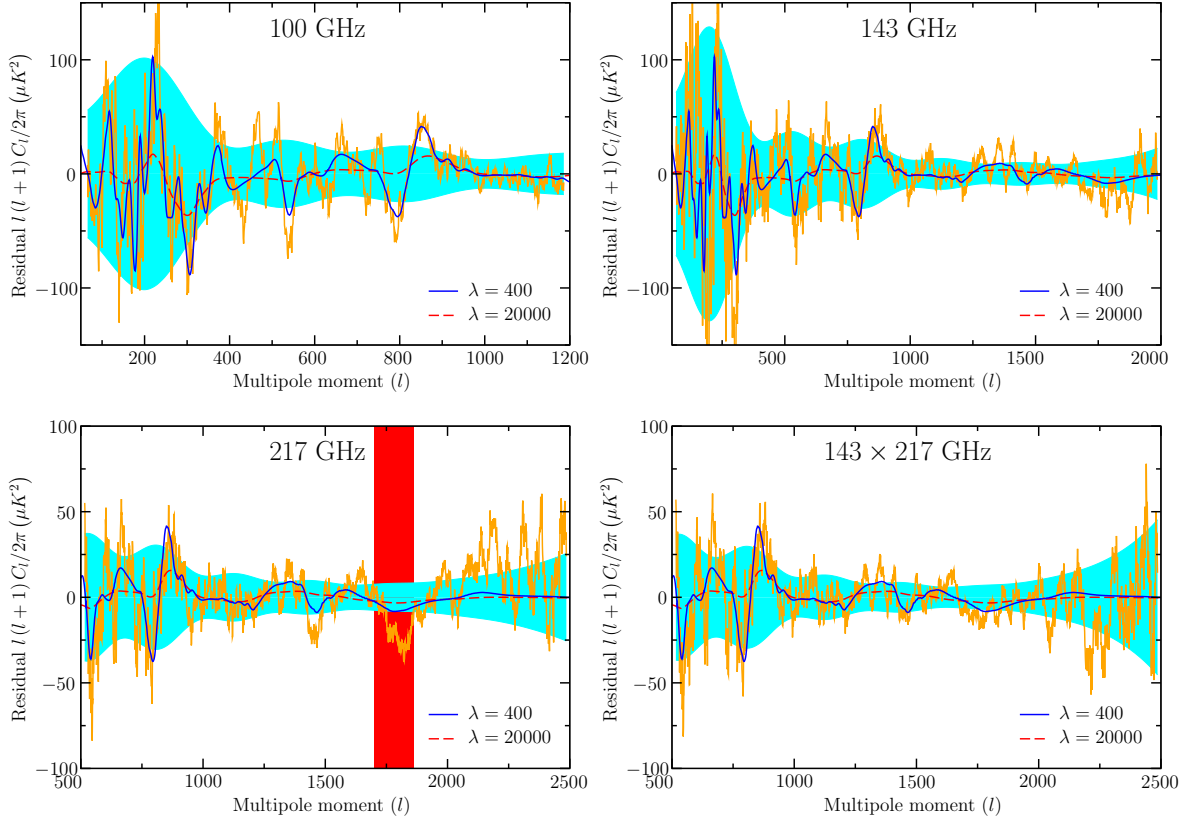


Figure 5. Comparison of residuals for the $\ell = 31$ running average of the Planck data (orange line) with the residuals corresponding to the $\lambda = 400$ (full blue line) and $\lambda = 20000$ (red dashed line) reconstructions from the Planck, WMAP-9 polarisation, ACT, SPT, WiggleZ, galaxy clustering, CFTHLenS and Lyman- α data (combination IV). The $\ell = 31$ running average is a series of averages of the data over 31 adjacent multipoles. The residuals are obtained by subtracting off the TT spectrum of the best-fit $n_s = 0.969$ power-law spectrum. The band indicates the 1σ scatter of the $\ell = 31$ running average data, calculated from the Planck covariance matrix. Top left: 100 GHz data. Top right: 143 GHz data. Bottom left: 217 GHz data (the vertical strip indicates the unused $1700 < \ell < 1860$ multipoles). Bottom right: 143×217 GHz data.

CMB likelihood function for low multipoles, as in [1].

To assess the evidence against the null hypothesis at a particular wavenumber k we use the *local* test statistic

$$T(k) \equiv \sum_i \frac{(\hat{p}_i - p_i^{\text{PL}})^2}{\sigma_i^2} \phi_i(k). \quad (3.2)$$

Here σ_i^2 is the variance of $\hat{p}_i - p_i^{\text{PL}}$, the deviation of the estimated PPS \hat{p}_i from the null hypothesis power-law PPS p_i^{PL} at wavenumber bin i . For a given wavenumber we compute the p -value of $T(k)$ (the probability under the null hypothesis of exceeding the observed test statistic value) using the distribution of $T(k)$ in the 10^6 simulated inversions⁴. The wavenumbers with the lowest p -values are recorded in Tables 2 and 3.

⁴On small scales where the CMB likelihood is Gaussian, the $T(k)$ statistic is χ^2 distributed to a high degree of accuracy.

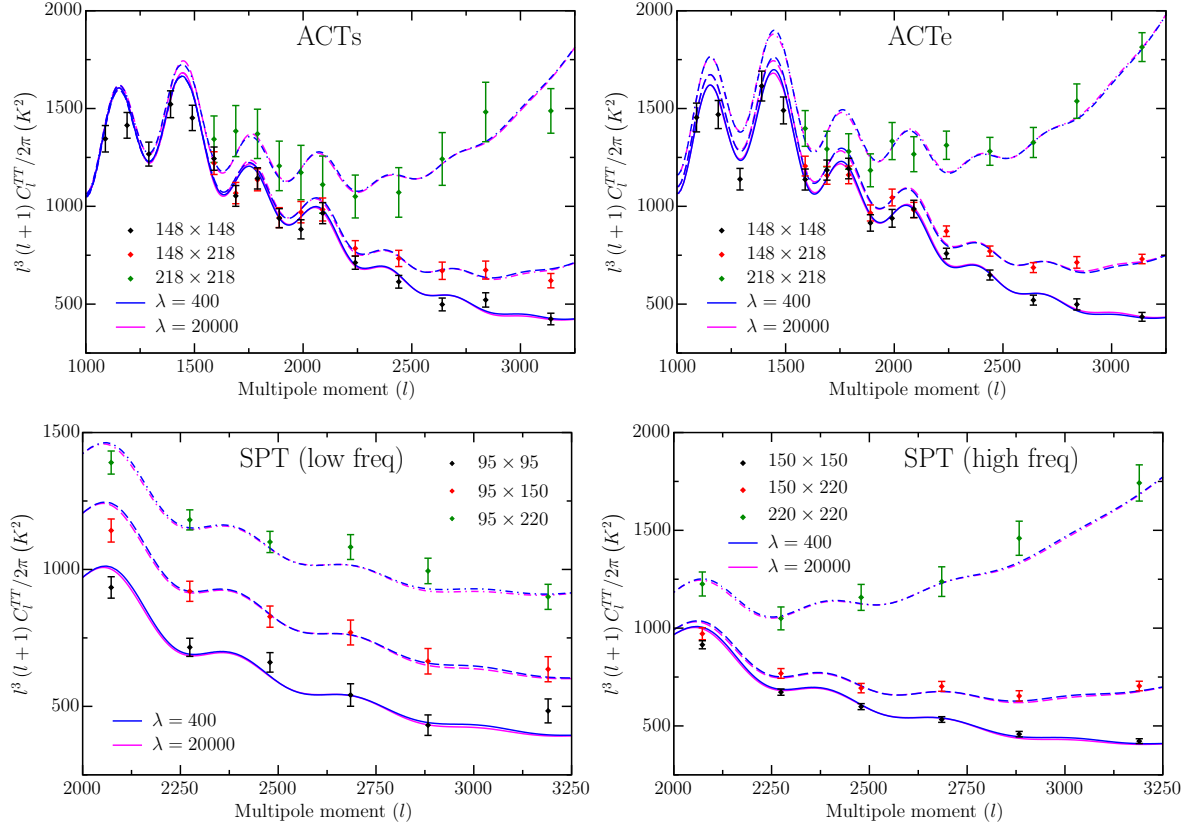


Figure 6. Fit to data from ACTs (top left), ACTe (top right), 95, 95 \times 150, 95 \times 220 GHz SPT (bottom left) and 150, 150 \times 220, 220 GHz SPT (bottom right) of power spectra recovered with $\lambda = 400$ and 20000 from the Planck, WMAP-9 polarisation, ACT, SPT, WiggleZ, galaxy clustering, CFTHLenS and Lyman- α data (combination IV). The 95 \times 150 and 95 \times 220 GHz SPT spectra have been shifted vertically (respectively by 250 and 500 K^2) for clarity.

For $\lambda = 400$ the peak at $k \simeq 0.12 \text{ Mpc}^{-1}$ represents a 4σ excursion, while the $k \simeq 0.057 \text{ Mpc}^{-1}$ dip and the $k \simeq 0.10 \text{ Mpc}^{-1}$ peak constitute 2.7σ and 2.8σ deviations respectively. All the other features have less than 2.4σ significance, including the dip at $k \simeq 0.0018 \text{ Mpc}^{-1}$ associated with the $\ell \simeq 22$ power deficit and the dip at $k \simeq 0.14 \text{ Mpc}^{-1}$ where the unreliable 217 GHz Planck spectrum is omitted. The statistical significance of the features in the $\lambda = 20000$ reconstruction is generally lower. The greatest departure from a power-law is the $k \simeq 0.14 \text{ Mpc}^{-1}$ dip at 2.9σ , up from 2.0σ for $\lambda = 400$.

While the $T(k)$ statistic can be used to gauge the significance of an individual feature, it must be remembered that over a sufficiently large wavenumber interval the $T(k)$ p -value will be small at some k purely by chance even if the null hypothesis is true. This is an example of the ‘look-elsewhere’ effect, or the problem of multiple comparisons, which is that the likelihood of a false detection of an anomaly increases with the size of parameter space searched. To account for this effect we use the *global* test statistic

$$T_{\max} \equiv \max_k T(k), \quad (3.3)$$

equal to the maximum value of $T(k)$ over the wavenumber range of the recovered PPS. Clearly if there are significant features *anywhere* in the PPS, T_{\max} will be greater than

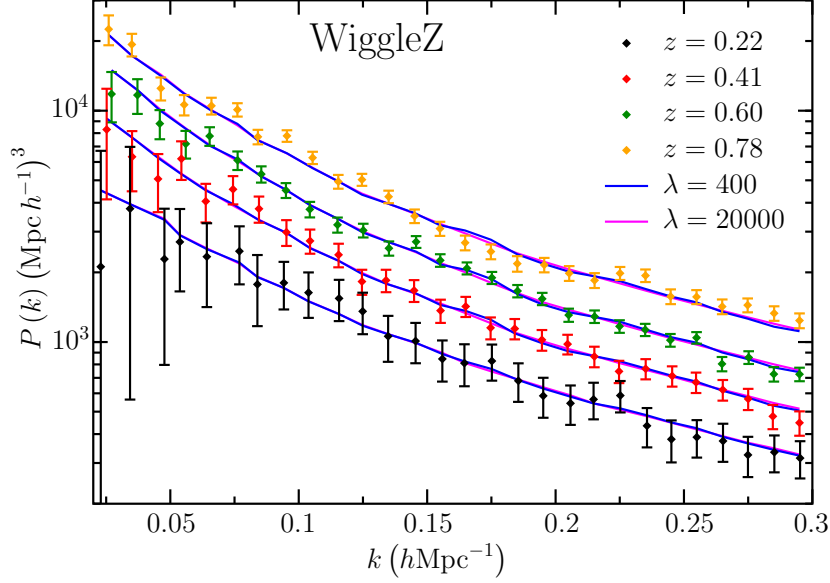


Figure 7. Fit to WiggleZ data (in 4 redshift bins) of power spectra recovered with $\lambda = 400$ and 20000 from the Planck, WMAP-9 polarisation, ACT, SPT, WiggleZ, galaxy clustering, CFTHLenS and Lyman- α data (combination IV), convolved with the WiggleZ window functions. Both data and theoretical predictions have been averaged over the 7 sky regions and shifted vertically for clarity (by a factor of 0.4, 0.6, 0.8 and 1.2 respectively for $z = 0.22, 0.41, 0.60$ and 0.78).

k/Mpc^{-1}	0.00177	0.0272	0.0390	0.0573	0.101
p -value	0.0291	0.0219	0.0364	0.00674	0.00471
Stat.sig./ σ	2.18	2.29	2.09	2.71	2.83

k/Mpc^{-1}	0.105	0.119	0.140	0.202	0.223
p -value	0.0203	5.40×10^{-5}	0.0474	0.0207	0.0304
Stat.sig./ σ	2.32	4.04	1.98	2.31	2.16

Table 2. $T(k)$ p -values of the highest significance features in the PPS recovered from data combination IV with $\lambda = 400$. The p -values are also converted to equivalent two-sided Gaussian standard deviations to express the statistical significance.

expected under the null hypothesis.⁵ The T_{\max} p -value for the *most* significant feature at $k \simeq 0.12 \text{ Mpc}^{-1}$, again computed using the simulations, is 0.0239 for $\lambda = 400$ and 0.172 for $\lambda = 20000$. This is equivalent to 2.26σ and 1.37σ respectively, hence both reconstructions of the scalar perturbations are statistically *consistent* with a power-law and there is no significant evidence presently for features in the PPS.

3.4 Tensor reconstruction

BICEP2 measured the CMB polarisation at 150 GHz over a small (380 square degree) region of sky near the South Galactic Pole and detected a B-mode polarisation signal around multipole $\ell \simeq 90$ in excess of that expected from lensed E-mode polarisation alone at 5.2σ

⁵A similar statistic has been studied previously in a different context [38, 39].

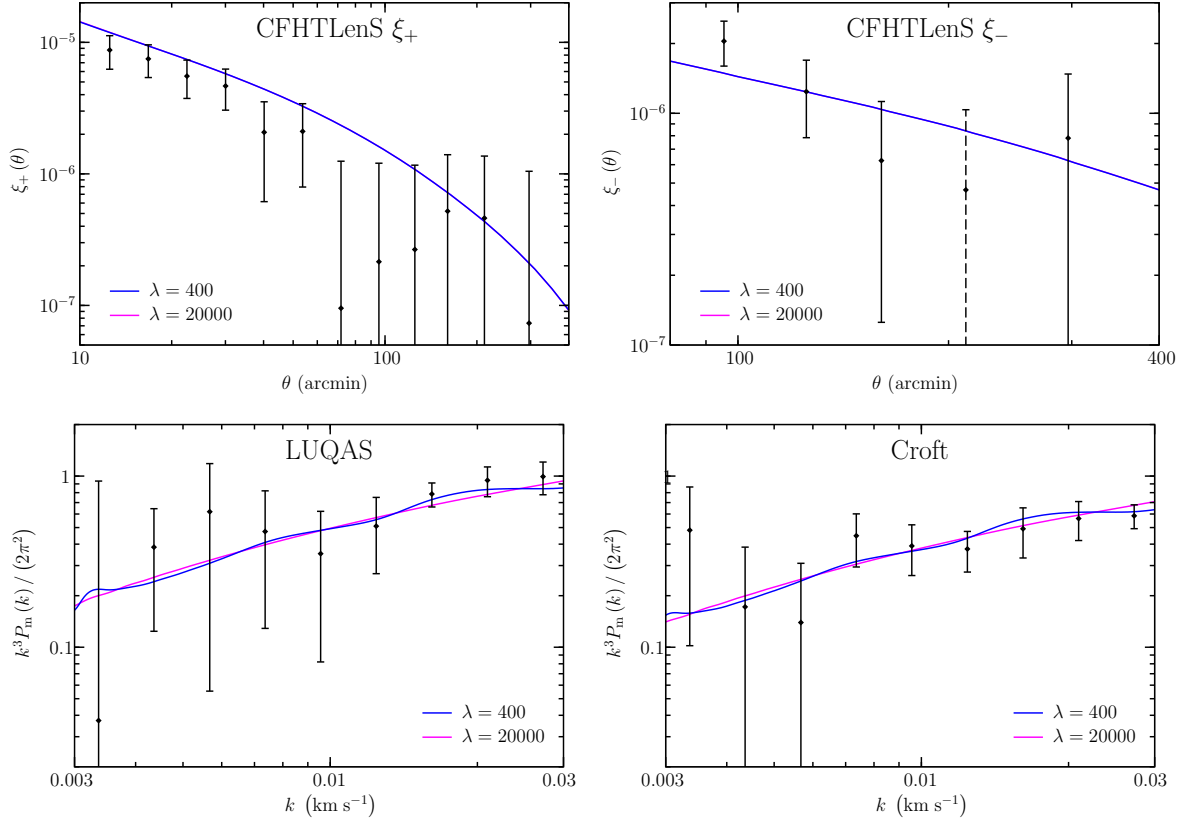


Figure 8. Fit to CFHTLenS shear correlation data $\xi_+(\theta)$ (top left) and $\xi_-(\theta)$ (top right), and Lyman- α data from LUQAS (bottom left) and Croft (bottom right), of power spectra recovered with $\lambda = 400$ and 20000 from the Planck, WMAP-9 polarisation, ACT, SPT, WiggleZ, galaxy clustering, CFHTLenS and Lyman- α data (combination IV). The $\xi_-(\theta)$ measurement at $\theta = 212'$ is *negative* (indicated by a dashed error bar).

k/Mpc^{-1}	0.0639	0.0873	0.0999	0.117	0.140
p -value	0.0902	0.140	0.100	0.0231	0.00398
Stat.sig./ σ	1.69	1.47	1.64	2.27	2.88

Table 3. Same as Table 2, but for $\lambda = 20000$.

significance [24]. The BICEP2 collaboration interpreted this as evidence for primordial gravitational waves with a tensor-to-scalar ratio of $r_{0.05} = 0.2^{+0.07}_{-0.05}$, ruling out $r_{0.05} = 0$ at 7σ significance (under the assumption that $n_t = 0$). Here the subscript on r indicates the scale (in Mpc^{-1}) at which r is defined. The BICEP2 result was surprising as the Planck team had previously reported $r_{0.002} < 0.11$ (95% CL) [9]. However, several authors then suggested that polarised galactic dust emission had been underestimated and could account for some or even all of the excess B-mode power.

For example it was noted that (polarised) magnetic dipole emission from radio loop S1 could be significant in the BICEP2 region of sky [73]. A joint analysis of the BICEP2 and Planck data, including a power-law dust template, yielded the upper limit $r_{0.05} < 0.11$ (95% CL), with $r_{0.05} = 0$ preferred [74]. It was emphasised that the BICEP2 measurements

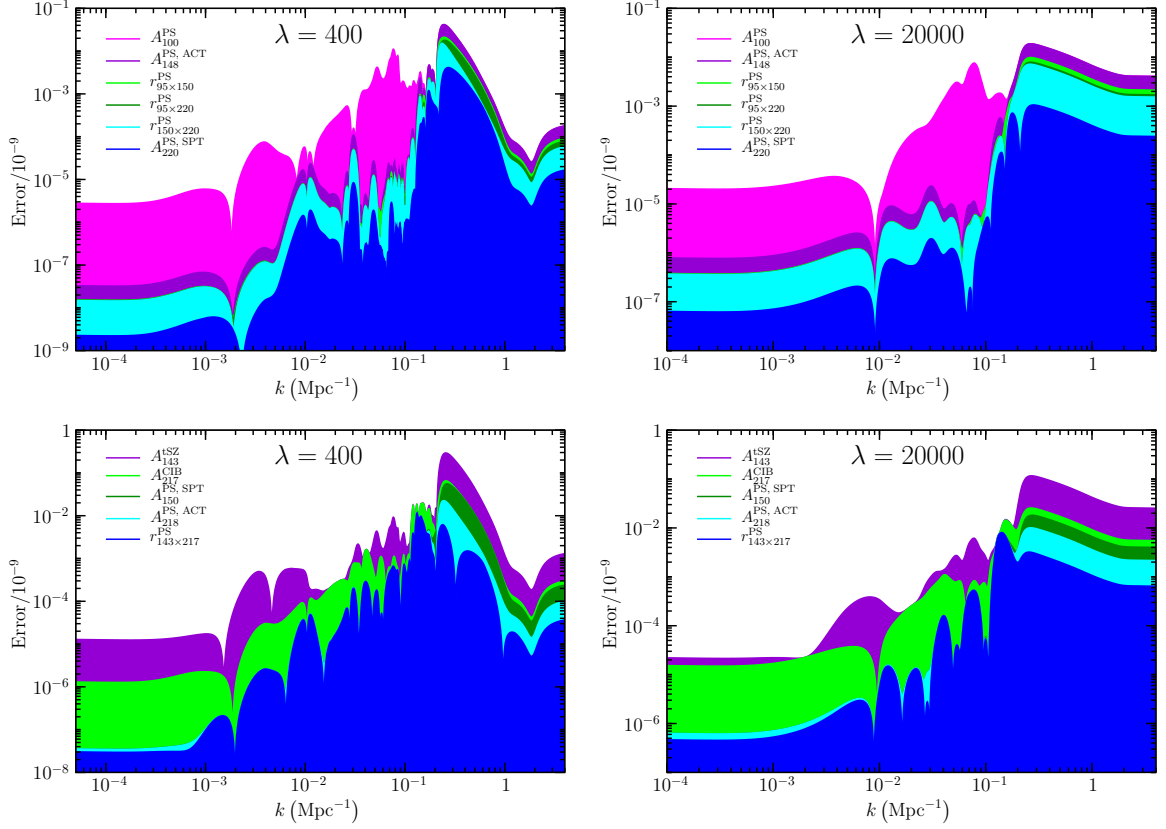


Figure 9. Contributions of some CMB foreground parameters to the square root of the diagonal elements of the matrix Σ_P (B.20) for Planck, WMAP-9 polarisation, ACT, SPT, WiggleZ, galaxy clustering, CFTHLenS and Lyman- α data (combination IV), with $\lambda = 400$ and 20000 . The error contributions are added in quadrature.

alone could not distinguish between gravitational waves and polarised dust, on the basis of 4 independent consistent estimates of the dust B-mode signal [75]. Using genus topology statistics it was concluded that $r = 0.11 \pm 0.04$ from a comparison of the BICEP2 B-mode map with a preliminary (dust-dominated) polarisation map at 353 GHz from Planck [76].

Subsequently Planck measured the EE and BB dust power spectra at intermediate and high Galactic latitudes over the range $40 < \ell < 600$ using polarisation maps at frequencies from 100 to 353 GHz [77]. Extrapolating the 353 GHz data to 150 GHz gave a BB dust power over the BICEP2 region of $0.0132 \pm 0.0040 \mu\text{K}^2$ in a bin centred at $\ell = 80$ (where the noise and extrapolation errors have been added in quadrature) which is comparable to the amplitude $0.0133 \pm 0.0017 \mu\text{K}^2$ of the BICEP2 BB bandpower at $\ell \simeq 74$. The Keck Array follow-up experiment confirmed the BICEP2 measurements at $> 5\sigma$ statistical significance and a joint BICEP2/Keck Array analysis was released [5], which we use in this paper. By cross-correlating the BICEP2/Keck Array and Planck results, an upper limit of $r_{0.05} < 0.12$ (95% CL) was set, with $r_{0.05} \simeq 0.05$ preferred [78].

In view of the current uncertainty in the dust component observed by BICEP2/Keck Array, we consider a range of values for the B-mode dust amplitude parameter A^{BB} in Eq.(A.42). This is similar in spirit to another analysis [40] where however the scalar and tensor spectra were assumed to be power laws. We perform joint reconstructions of $\mathcal{P}_{\mathcal{R}}(k)$

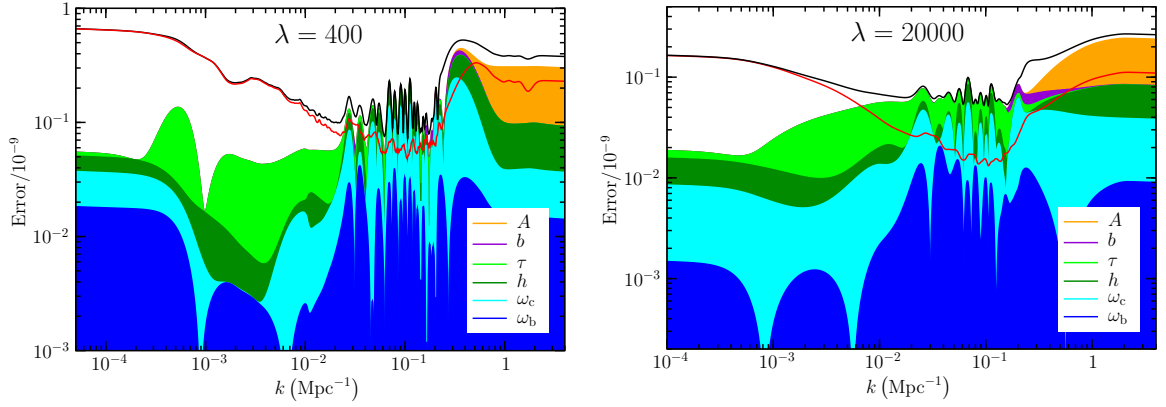


Figure 10. Contributions of different background parameters to the square root of the diagonal elements of the matrix Σ_P (B.20) Planck, WMAP-9 polarisation, ACT, SPT, WiggleZ, galaxy clustering, CFTHLenS and Lyman- α data (combination IV). The error contributions are added in quadrature. In the left panel $\lambda = 400$ and in the right panel $\lambda = 5000$. In both panels the red line is the square root of the diagonal elements of the matrix Σ_F (B.19) and is included for comparison. The black line is the square root of the diagonal elements of the matrix Σ (B.18). It includes contributions to the total error from uncertainties in the background and nuisance parameters, as well as from noise in the data.

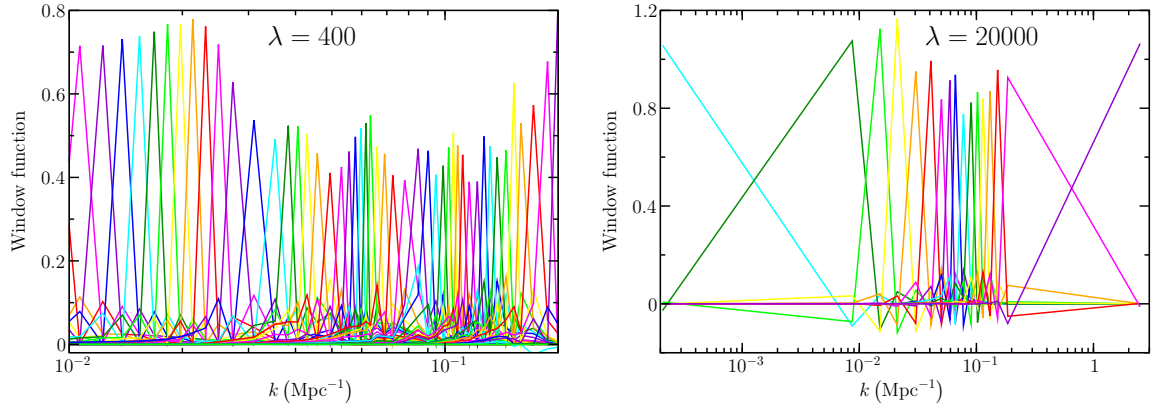


Figure 11. Bandpower window functions for $\lambda = 400$ and 20000 of reconstructions using the Planck, WMAP-9 polarisation, ACT, SPT, WiggleZ, galaxy clustering, CFTHLenS and Lyman- α data (combination IV).

and $\mathcal{P}_h(k)$ from data combination V with $\lambda = 400$ for the parameters listed in Table 4.

The roughness penalty function $R_t(\mathbf{z})$ increases as the amplitude of the tensor spectrum falls (recall that $z_i = \ln q_i$). Increasing the dust power reduces the amplitude of the tensor spectrum required to fit the BICEP2/Keck Array data. Therefore the recovered tensor spectra will become increasingly oversmoothed. In order to present a fair comparison we must ensure the level of smoothing remains constant as the dust power varies. To achieve this we incorporate the parameter $c_{\text{dust}} \equiv (\hat{\mathbf{z}}_{\text{no-dust}}/\hat{\mathbf{z}}_{\text{dust}})^2$ into Eq.(2.16). Here $\hat{\mathbf{z}}_{\text{no-dust}}$ and $\hat{\mathbf{z}}_{\text{dust}}$ are the tensor spectra recovered (with $c_{\text{dust}} = 1$) in the absence and presence of dust respectively. We evaluate c_{dust} at the scale $k = 0.01 \text{ Mpc}^{-1}$. In this way we effectively normalise the tensor penalty function each time to that of the no dust case.

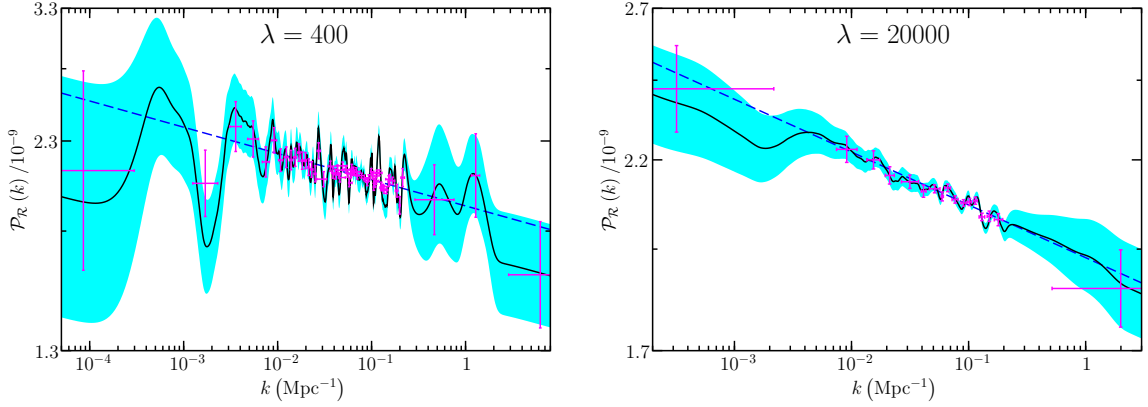


Figure 12. Decorrelated bandpowers for $\lambda = 400$ and 20000 . The black line is the PPS recovered from the Planck, WMAP-9 polarisation, ACT, SPT, WiggleZ, galaxy clustering, CFTHLenS and Lyman- α data (combination IV). The light band is the 1σ error obtained from the square root of the diagonal elements of the frequentist covariance matrix Σ_F (B.19). The vertical error bars are the 1σ errors given by the diagonal bandpower covariance matrix. The horizontal error bars indicate the locations of the 25th and 75th percentiles of the absolute value of the bandpower window functions.

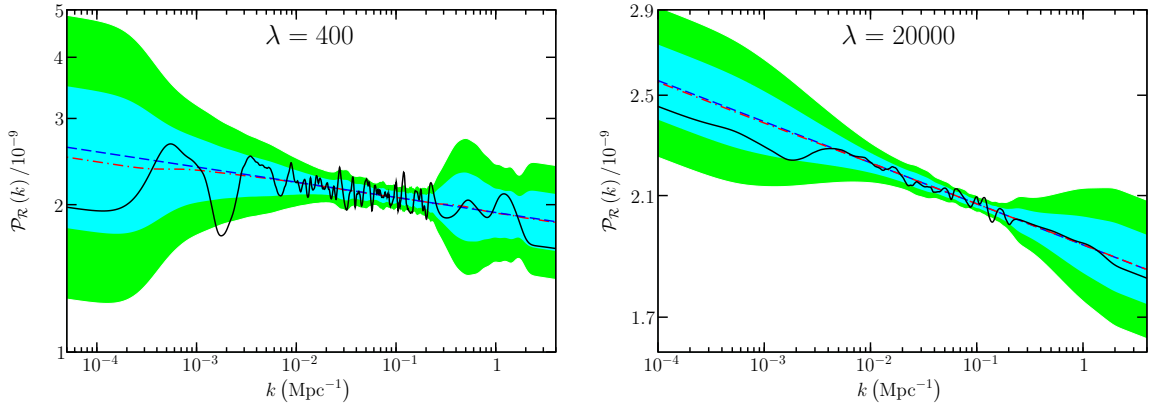


Figure 13. Comparison of the PPS recovered from the Planck, WMAP-9 polarisation, ACT, SPT, WiggleZ, galaxy clustering, CFTHLenS and Lyman- α data (combination IV, full black line) with the results of 10^6 simulated reconstructions for $\lambda = 400$ and 20000 which were generated using a power-law PPS with $n_s = 0.969$ (dashed blue line). The shaded bands indicate the 1σ and 2σ error estimate from Monte Carlo simulations, while the red dot-dashed line is the mean of the reconstructions.

Single-field slow-roll models of inflation satisfy the consistency relation $n_t = -r/8$ to first order in the slow-roll parameters. The predicted slope is *negative* because the amplitude of tensor perturbations is proportional to the Hubble parameter at horizon exit, and larger scales exit earlier during inflation when the Hubble parameter is greater.⁶ To include this as a prior on our joint reconstructions we set $n_t = -r_{0.01}/8$ in Eq.(2.14) at each iteration of the Newton-Raphson minimisation of $Q(\mathbf{Y}, \mathbf{d}, \hat{\theta}, \lambda)$. This is feasible because $r_{0.01}$ is well

⁶However there are exotic models with non-Bunch-Davies initial conditions [45], violation of the null energy condition [46], particle production during inflation [47] or other novel features [44, 48] that do give $n_t > 0$. Some non-inflationary cosmological models also predict a blue tensor spectrum [49–51].

constrained by the data and largely independent of the prior n_t value.

The fit to the BICEP2/Keck Array measurements are shown in Fig.14 and the recovered power spectra in Fig.15. The tensor spectrum with 0% dust is best constrained at $k \simeq 0.01 \text{ Mpc}^{-1}$ by the BICEP2/Keck Array data where the resolution of the reconstruction is greatest, as shown in Fig.20. The recovered tensor spectrum has a strong *positive* slope (a blue tilt) at $k \simeq 0.01 \text{ Mpc}^{-1}$ due to the BICEP2/Keck Array measurements and a flat plateau on larger scales due to the Planck and WMAP-9 polarisation observations, with a dip at $k \simeq 0.0018 \text{ Mpc}^{-1}$ caused by the TT power deficit at $\ell \simeq 22$. Including the WMAP-9 measurements suppresses the recovered tensor spectrum on large scales because the low ℓ BB data are consistent with $r = 0$ [41]. Since the tensor perturbations contribute to the TT angular power spectrum for $\ell \lesssim 150$ the recovered scalar spectrum is suppressed for $k \lesssim 0.01 \text{ Mpc}^{-1}$ relative to the reconstruction without tensors. This had previously been noted in e.g. [15, 16, 42].

We report in Table 4 the tensor spectral index n_t^{fit} of the best-fit power-law PPS (with a pivot scale of $k_* = 0.01 \text{ Mpc}^{-1}$) to the recovered tensor spectrum over $0.003 \leq k \leq 0.03 \text{ Mpc}^{-1}$. For comparison [40] found $n_t = 1.8 \pm 0.6$ for a power-law tensor spectrum from the Planck, WMAP-9 polarisation and BICEP2 data with all 9 bandpowers, while [43] deduced $n_t = 1.36 \pm 0.83$ from the 9 BICEP2 bandpowers alone. However $n_t = 0.03 \pm 1.14$ was reported using only the first 5 BICEP2 bandpowers [44]; we believe a larger blue tilt would have been obtained had the Planck and WMAP-9 polarisation measurements been included as well. Note also that the BICEP2/Keck Array data [5] prefer a steeper positive slope than the earlier BICEP2 results [24]. This is because the first three BB bandpowers are lower and the uncertainty in the high amplitude fifth bandpower is reduced. The tensor spectrum found in [16] from Planck and the 5 lowest BICEP2 bandpowers using a 3 knot cubic spline method also has a positive slope but flattens at the slightly lower scale of $k \simeq 0.01 \text{ Mpc}^{-1}$ rather than $k \simeq 0.03 \text{ Mpc}^{-1}$ in our reconstruction. It also has no flat plateau on large scales. We attribute these differences to the relatively low number of knots employed by these authors.

Increasing the dust power reduces the amplitude of the recovered tensor spectrum, in accordance with expectation. The positive slope increases because the EE and BB dust angular power spectra in Eq.(A.42) fall with ℓ , as shown in Fig.15. Therefore increasing the dust amplitude A^{BB} causes the tensor spectrum on large scales to decrease more than the spectrum on small scales. The uncertainty in the recovered tensor spectrum also increases with the dust power. All this makes it even more likely that BICEP2 observed dust rather than primordial tensor perturbations and demonstrates the advantage of a consistent *joint* reconstruction of the scalar and tensor spectrum.

4 Conclusions

The generation of large-scale structure in the universe by growth of initially small density fluctuations through gravitational instability is akin to a scattering experiment at a high energy accelerator. The ‘beam’ here corresponds to the primordial perturbations, the ‘target’ to the (mainly dark) matter content of the universe, and the ‘detector’ to the universe as a whole, while the ‘signal’ is the CMB anisotropy or galaxy correlations. In contrast to the laboratory situation where the only unknown is the physical interaction between the beam and the target, in the cosmological context this is known to be gravity. However all else is unknown or uncertain. We cannot *simultaneously* infer the properties of the target and the detector with an unknown beam, hence there are ‘degeneracies’ and necessarily circularity

Dust fraction	$10^3 A^{\text{BB}}/\mu\text{K}^2$	$r_{0.01}$	c_{dust}	$10^2 n_{\text{t}}^{\text{prior}}$	$n_{\text{t}}^{\text{fit}}$
0.00	0.00	0.173	1.00	-2.17	0.44 ± 0.21
0.25	2.57	0.132	0.63	-1.65	0.56 ± 0.26
0.50	5.13	0.094	0.40	-1.18	0.66 ± 0.33
0.75	7.70	0.061	0.23	-0.76	0.74 ± 0.43

Table 4. Parameters associated with the joint scalar and tensor power spectra reconstructions. The B-mode dust power is expressed as a fraction of the BICEP2/Keck Array bandpower at $\ell \simeq 74$. The B-mode dust amplitude parameter A^{BB} is defined in Eq.(A.42), while $r_{0.01}$ is the tensor-to-scalar ratio of the recovered spectra at $k = 0.01 \text{ Mpc}^{-1}$. The quantity c_{dust} ensures that the tensor spectra recovered with the different A^{BB} values are equally smoothed. The prior tensor spectral index $n_{\text{t}}^{\text{prior}} \equiv -r_{0.01}/8$ is used in the penalty function (2.14) and $n_{\text{t}}^{\text{fit}}$ is obtained by fitting the recovered tensor spectrum over $0.003 \leq k \leq 0.03 \text{ Mpc}^{-1}$ to a power-law with a pivot scale of $k_* = 0.01 \text{ Mpc}^{-1}$.

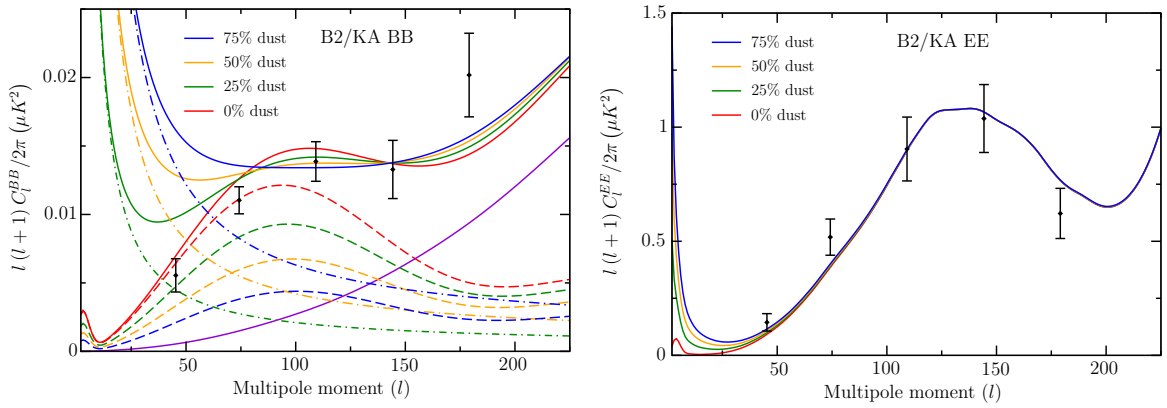


Figure 14. Left: the BB angular power spectra (dashed red, green, orange and blue lines) recovered (with $\lambda = 400$) from data combination V (BICEP2/Keck Array, Planck, WMAP-9 polarisation, ACT, SPT + cluster abundance and WiggleZ), assuming various levels of dust contamination. The solid purple line indicates the lensed EE contribution and the dot-dashed lines represent the dust power spectra with the scaling $C_{\ell, \text{dust}}^{\text{BB}} \propto \ell^{-2.42}$ estimated by Planck. The solid red, green, orange and blue lines are the total BB spectra. Right: the total EE spectra, which are dominated by the scalar contribution (except at very low ℓ), compared to the BICEP2/Keck Array data.

in e.g. inferring cosmological parameters (the ‘detector’) or the nature of the dark matter (the ‘target’) or the spectrum of the density fluctuations (the ‘beam’). It is common in particular for the spectrum to be taken to be a power-law and the dark matter to be cold and collisionless, in determining the parameters of the assumed ΛCDM cosmology.

A consistency check would be to reverse this procedure and attempt to infer the PPS, as we have done following our method detailed earlier [1], using Planck [2] and other CMB and large-scale structure data sets. We find several features in the spectrum, of which one has significance $\gtrsim 4\sigma$. This is potentially of great interest as such features cannot be generated in the standard slow-roll models of inflation driven by a scalar field. However the feature is suspect (even though it is in the supposedly clean 143x217 GHz spectrum) as it is associated with the same multipole range $1700 < \ell < 1860$ as the 217x217 GHz contamination. Hence we cannot claim that it is primordial in origin. In addition its significance drops to $\sim 2\sigma$ after we account for the ‘look elsewhere’ effect, hence there is *no* compelling evidence for a departure of the scalar fluctuations from a power-law spectrum. Moreover our simultaneous

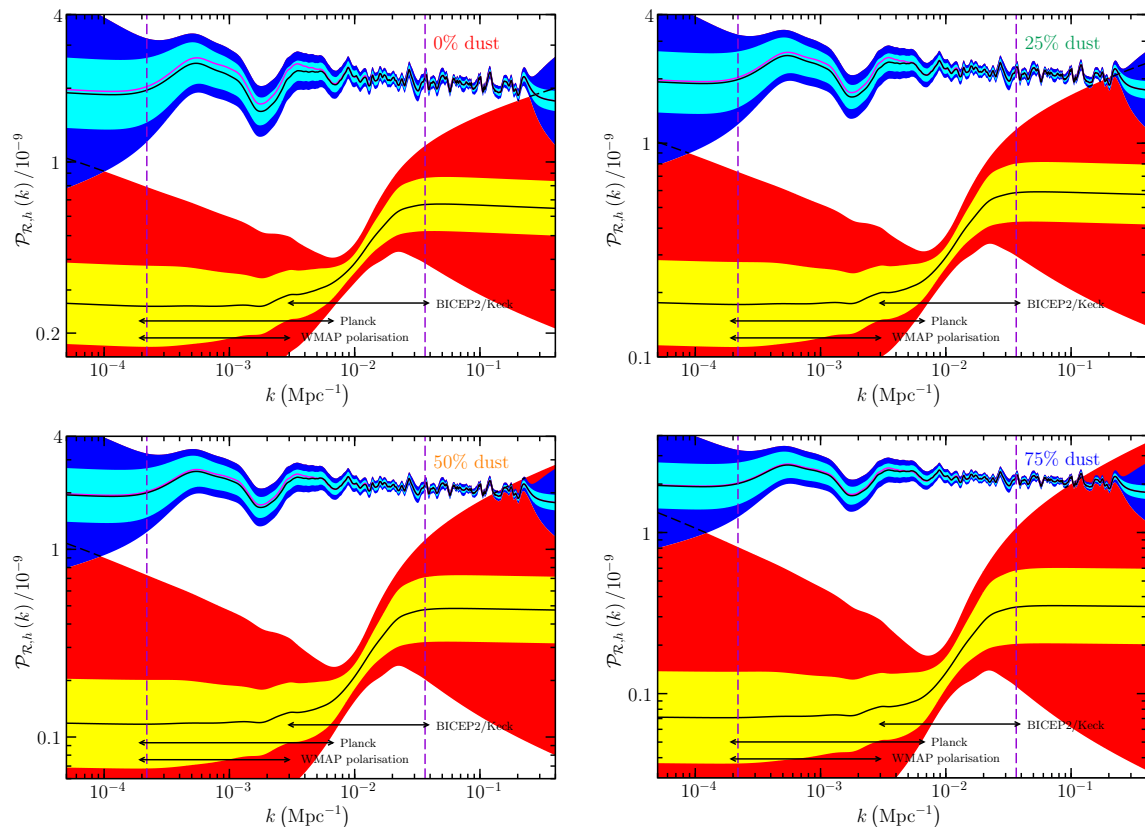


Figure 15. The scalar and tensor perturbation spectra (black lines) recovered from the BICEP2/Keck Array, Planck, WMAP-9 polarisation, ACT, SPT, WiggleZ, galaxy clustering, CFTHLenS and Lyman- α data (data combination V) with $\lambda = 400$, assuming various levels of dust contamination in the BICEP2/Keck Array data, and with priors $n_s = 0.969$ and $n_t = -r/8$. In all plots the magenta line is the scalar spectrum in the absence of tensor perturbations. The light bands are the 1σ error given by the square root of the diagonal elements of the joint frequentist covariance matrix Σ_F (B.23), while the larger dark bands are similarly obtained from the joint Bayesian covariance matrix Π . Vertical lines delineate the wavenumber range covered by the resolution kernels (see Fig.20) over which the reconstruction is faithful to the true tensor PPS, while the horizontal lines indicate the range over which specific datasets have most impact. Note the unexpected *positive* slope of the tensor perturbation spectrum according to BICEP2/Keck.

reconstruction of the tensor fluctuation spectrum using the BICEP2/Keck data on B-mode polarisation in the CMB [5] reveals that it has a blue rather than red slope as is expected in slow-roll models, making it even more likely that it is emission by dust.

Thus both of our conclusions are negative. Nevertheless we believe that searches for spectral features are still the best direct probe of inflation, especially given the lack of evidence for any non-gaussianity in the CMB and the well recognised difficulties in searches for the B-mode polarisation signal from inflationary gravitational waves. In contrast to the latter signatures, the TT signal is orders of magnitude higher, with systematics that can in principle be better understood. Hence we intend to continue such searches with further data releases from Planck and other CMB experiments, as well as data from observational probes of large-scale structure in the universe, which can be consistently analysed together in our framework.

Acknowledgements

We acknowledge use of the **CAMB** and **cosmoMC** codes and thank the Planck team for making their data and analysis tools publicly available. PH is grateful to the Niels Bohr Institute for hospitality and SS acknowledges a DNRF Niels Bohr Professorship and helpful discussions with Pavel Naselsky.

A Data sets

We discuss the data sets used in our analysis; throughout we have treated the data *exactly* as recommended by the experimental collaboration which provided it.

A.1 Planck

The Planck temperature likelihood function L_{Planck} is a hybrid combination of a Gibbs sampler based Blackwell-Rao estimator L_{Comm} implemented in the **Commander** software code for $2 \leq \ell \leq 49$, and a Gaussian pseudo- C_ℓ approximation L_{CamSpec} for $50 \leq \ell \leq 2500$ computed by the **CamSpec** code [2]. Thus $L_{\text{Planck}} = L_{\text{Comm}} + L_{\text{CamSpec}}$. The **Commander** likelihood uses a low-resolution, foreground-cleaned combination of the seven maps from 30 to 353 GHz, while the **CamSpec** likelihood uses cross-spectra from the 100, 143 and 217 GHz channels. The multipole range for the 100×100 GHz and 143×143 GHz spectra is $50 \leq \ell \leq 1200$ and $50 \leq \ell \leq 2000$ respectively, while the 217×217 GHz and 143×217 GHz spectra both cover $500 \leq \ell \leq 2500$. The **CamSpec** likelihood is [52]

$$L_{\text{CamSpec}} = \sum_{\ell\ell'} \sum_{II'} \left(\frac{s_\ell^{\text{TT}} + f_\ell^I}{\sigma_\ell^I} - d_\ell^I \right) (N_{\ell\ell'}^{-1})^{II'} \left(\frac{s_{\ell'}^{\text{TT}} + f_{\ell'}^{I'}}{\sigma_{\ell'}^{I'}} - d_{\ell'}^{I'} \right), \quad (\text{A.1})$$

where the index I labels the spectrum, i.e. $I \in \{100 \times 100, 143 \times 143, 217 \times 217, 143 \times 217\}$. Here s_ℓ^{TT} is the theoretical temperature angular power spectrum and d_ℓ^I is the measured I th cross-spectrum. The covariance matrices $N_{\ell\ell'}^{II'}$ incorporate the correlations between the different spectra and are evaluated for a fixed fiducial model. The f_ℓ^I terms represent the unresolved ‘foreground’ which can include galactic point sources, clustered sources in the cosmic infrared background (CIB), and the kinetic and thermal Sunyaev-Zeldovich effects (kSZ and tSZ) from galaxy clusters, as discussed in [2, 9]. They are given by

$$f_\ell^{100 \times 100} = A_{100}^{\text{PS}} \tilde{\ell}^2 + A^{\text{kSZ}} t_\ell^{\text{kSZ}} + c_1 A^{\text{tSZ}} t_\ell^{\text{tSZ}}, \quad (\text{A.2})$$

$$f_\ell^{143 \times 143} = A_{143}^{\text{PS}} \tilde{\ell}^2 + A^{\text{kSZ}} t_\ell^{\text{kSZ}} + c_2 A^{\text{tSZ}} t_\ell^{\text{tSZ}} + c_3 A_{143}^{\text{CIB}} \tilde{\gamma}^{\text{CIB}} - 2 (c_2 c_3 A_{143}^{\text{CIB}} A^{\text{tSZ}})^{1/2} \xi^{\text{tSZ} \times \text{CIB}} t_\ell^{\text{tSZ} \times \text{CIB}}, \quad (\text{A.3})$$

$$f_\ell^{217 \times 217} = A_{217}^{\text{PS}} \tilde{\ell}^2 + A^{\text{kSZ}} t_\ell^{\text{kSZ}} + c_4 A_{217}^{\text{CIB}} \tilde{\gamma}^{\text{CIB}}, \quad (\text{A.4})$$

$$f_\ell^{143 \times 217} = r_{143 \times 217}^{\text{PS}} (A_{143}^{\text{PS}} A_{217}^{\text{PS}})^{1/2} \tilde{\ell}^2 + A^{\text{kSZ}} t_\ell^{\text{kSZ}} + r_{143 \times 217}^{\text{CIB}} (c_3 c_4 A_{143}^{\text{CIB}} A_{217}^{\text{CIB}})^{1/2} \tilde{\gamma}^{\text{CIB}} - (c_3 c_4 A_{217}^{\text{CIB}} A^{\text{tSZ}})^{1/2} \xi^{\text{tSZ} \times \text{CIB}} t_\ell^{\text{tSZ} \times \text{CIB}}, \quad (\text{A.5})$$

where $\tilde{\ell} \equiv \ell/3000$. Here t_ℓ^{kSZ} , t_ℓ^{tSZ} and $t_\ell^{\text{tSZ} \times \text{CIB}}$ are theoretical ‘templates’ for the kSZ and tSZ components, and for the tSZ and CIB cross-correlation (which are fixed for the present analysis) [2]. The constants c_1 to c_4 (all of order unity) correct for the different

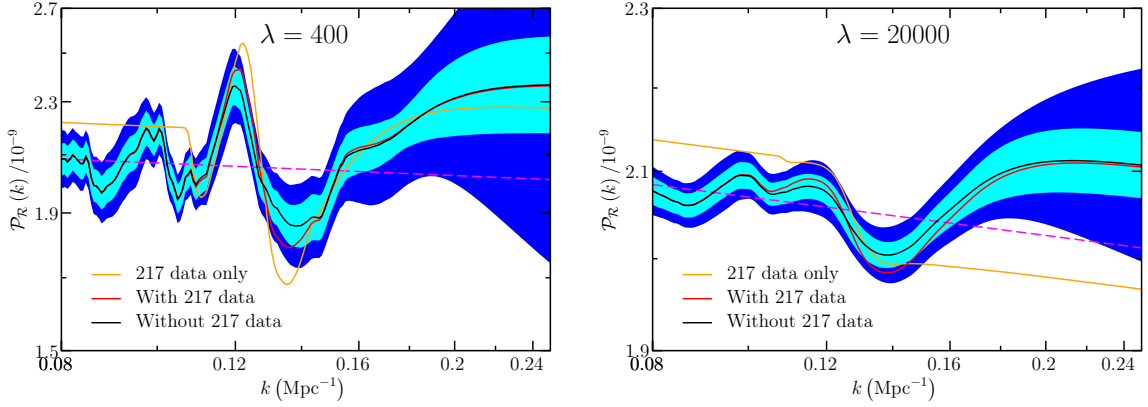


Figure 16. The PPS recovered from the Planck data with (red line) and without (black line) the 217 GHz data over the $1700 < \ell < 1860$ multipoles, with $\lambda = 400$ (left) and $\lambda = 20000$ (right). The orange line is the PPS recovered from the 217 GHz $1500 < \ell < 2060$ multipoles alone, while the dashed magenta line is the best-fit power-law with $n_s = 0.969$. Removing the contaminated 217 GHz data does reduce the amplitude of the $k = 0.14 \text{ Mpc}^{-1}$ feature, but it still remains significant.

bandpass responses of the Planck detectors, while the remaining 11 parameters characterise the amplitudes and cross-correlations of the various foreground components.

Beam and calibration errors are responsible for the following terms in the likelihood:

$$\sigma_\ell^I = C_I \left(1 + \beta_1^{100 \times 100} \sum_i g_i^I E_{i\ell}^I \right)^{-1}. \quad (\text{A.6})$$

Here C_I are the calibration factors for the different spectra, with $C_{143 \times 143} = 1$ and $C_{143 \times 217} = C_{217 \times 217}^{1/2}$, so that only $C_{100 \times 100}$ and $C_{217 \times 217}$ are free parameters. Uncertainties in the beam transfer functions are parameterised by the beam error eigenmodes $E_{i\ell}^I$ [53]. All of the beam eigenmode amplitudes apart from $\beta_1^{100 \times 100}$ (the first of the 100×100 beam eigenmodes) are marginalised over analytically. This gives rise to the second factor above where g_i^I are the beam conditional means, with $g_1^{100 \times 100} = 1$.

Electromagnetic interference between the Planck satellite 4K Joule-Thomson cryogenic cooler and the HFI bolometers produces discrete ‘lines’ in the power spectral density of the time-ordered data, which manifest as features at certain multipoles in the measured angular power spectrum [54]. As first suggested in [22] and later confirmed by the Planck team [9], the correction for the 4K cooler lines was imperfect, leading to an artificial dip at $\ell \simeq 1800$ in the 217×217 GHz cross-spectrum. We therefore exclude the 217×217 GHz data over the interval $1700 < \ell < 1860$ when performing our reconstructions. Fig.16 shows that the effect of removing the data is to reduce the amplitude of the peak at $k = 0.12 \text{ Mpc}^{-1}$ and the dip at $k = 0.14 \text{ Mpc}^{-1}$ in the recovered PPS.

Both the derivative $\partial L_{\text{Comm}} / \partial y_i$, which is evaluated numerically, and the Hessian $\partial^2 L_{\text{Comm}} / \partial y_i \partial y_j$ are required in order to obtain $\hat{\mathbf{y}}$. Now, for $\ell < 50$ we use the expression

$$(N^{\text{TT}})^{-1}_{\ell\ell} = \frac{(2\ell + 1) f_{\text{sky}}^2}{2 (s_\ell^{\text{TT}} + \mathcal{N}_\ell^{\text{TT}})^2}, \quad (\text{A.7})$$

for the diagonal elements of the inverse TT covariance matrix, where $f_{\text{sky}} = 0.8$ is the effective fraction of the sky covered by Planck. To estimate the TT noise spectrum we employ

$$\frac{1}{\mathcal{N}_\ell^{\text{TT}}} = \sum_\nu \frac{1}{(\Delta_\nu^{\text{TT}} \theta_\nu)^2} \exp \left[-\frac{\ell(\ell+1)\theta_\nu}{8 \ln 2} \right], \quad (\text{A.8})$$

valid for an idealised CMB experiment with Gaussian beams and isotropic Gaussian white noise. Here ν is the frequency of the band, θ_ν is the beam width and Δ_ν^{TT} is the temperature noise per pixel. Following [80] we include only the 3 channels (100, 143 and 217 GHz) least affected by foreground contamination and assume they have been perfectly cleaned. Their specifications are listed in Table 5. The subdominant off-diagonal elements of the covariance matrix are neglected. The Hessian is then approximated by $\partial^2 L_{\text{Comm}} / \partial y_i \partial y_j \simeq 2 \sum_{\ell\ell'} \mathbf{p}_i W_{\ell i}^{\text{TT}} (N^{\text{TT}})^{-1}_{\ell\ell'} W_{\ell j}^{\text{TT}} \mathbf{p}_j$, which holds for a Wishart (or Gaussian) likelihood function.

ν/GHz	θ_ν	$\Delta_\nu^{\text{TT}}/\mu\text{K}$
100	9.6'	8.2
143	7.0'	6.0
217	4.6'	13.1

Table 5. Technical details for the 100, 143 and 217 GHz channels of the Planck HFI [81].

A.2 ACT

ACT measures CMB anisotropies at frequencies including 148 and 218 GHz in two separate regions of the sky — an equatorial strip (ACTe) and a southern strip (ACTs) [3, 55]. Hence the total likelihood is $L_{\text{ACT}} \equiv L_{\text{ACTe}} + L_{\text{ACTs}}$ where

$$L_{\text{ACTe/s}} = \sum_{bb'} \sum_{II'} \sum_{\alpha\alpha'} \left(\frac{s_b^I + f_b^I}{\sigma^I} - d_b^{I\alpha} \right) (N_{bb'}^{-1})^{II'}_{\alpha\alpha'} \left(\frac{s_{b'}^{I'} + f_{b'}^{I'}}{\sigma^{I'}} - d_{b'}^{I'\alpha'} \right). \quad (\text{A.9})$$

Here $I \in \{148 \times 148, 148 \times 218, 218 \times 218\}$ labels the three cross-frequency pairs used in the likelihood. ACT measured bandpowers (labelled b) in bands of multiple ℓ , with window functions $W_{b\ell}^I$, thus $s_b^I = \sum_\ell W_{b\ell}^I s_\ell^{\text{TT}}$. The 148×148 GHz bandpowers lie in the range $1000 \leq \ell \leq 3250$, while the 148×218 and 218×218 GHz bandpowers cover $1500 \leq \ell \leq 3250$. We do not use higher multipole bandpowers as secondary CMB anisotropies dominate over the PPS-dependent primary anisotropies on such small scales. ACTe (ACTs) data was collected over two (three) seasons of observations, hence the bandpower measurements $d_b^{I\alpha}$ are labelled both by pairs of seasons (the index α) and pairs of frequencies (the index I). For ACTe there are three different season pairs for the 148×148 and 218×218 GHz bandpowers, and four season pairs for the 148×218 GHz bandpowers, leading to a total of 10 bandpower sets. For ACTs there are 21 bandpower sets as there are six season pairs for the 148×148 and 218×218 GHz bandpowers, and nine season pairs for the 148×218 GHz bandpowers.

The ACT foreground model is the same as the one used for Planck, therefore

$$\begin{aligned} f_\ell^{148 \times 148} &= A_{148}^{\text{PS, ACT}} \tilde{\ell}^2 + A^{\text{kSZ}_\ell \text{kSZ}} + c_5 A^{\text{tSZ}_\ell \text{tSZ}} + c_6^2 A_{143}^{\text{CIB}} \tilde{\ell}^{\gamma^{\text{CIB}}} \\ &\quad + c_7^2 A_{\text{dust}}^{\text{ACTe}} \tilde{\ell}^{-0.7} - 2c_6 (c_5 A_{143}^{\text{CIB}} A^{\text{tSZ}})^{1/2} \xi^{\text{tSZ} \times \text{CIB}} t_\ell^{\text{tSZ} \times \text{CIB}}, \end{aligned} \quad (\text{A.10})$$

$$\begin{aligned} f_\ell^{148 \times 218} &= r_{150 \times 220}^{\text{PS}} \left(A_{148}^{\text{PS, ACT}} A_{218}^{\text{PS, ACT}} \right)^{1/2} \tilde{\ell}^2 + A^{\text{kSZ}_\ell \text{kSZ}} \\ &\quad + c_6 c_8 r_{143 \times 217}^{\text{CIB}} (A_{143}^{\text{CIB}} A_{217}^{\text{CIB}})^{1/2} \tilde{\ell}^{\gamma^{\text{CIB}}} + c_7 c_9 A_{\text{dust}}^{\text{ACTe}} \tilde{\ell}^{-0.7} \\ &\quad - c_8 (c_5 A_{217}^{\text{CIB}} A^{\text{tSZ}})^{1/2} \xi^{\text{tSZ} \times \text{CIB}} t_\ell^{\text{tSZ} \times \text{CIB}}, \end{aligned} \quad (\text{A.11})$$

$$f_\ell^{218 \times 218} = A_{218}^{\text{PS, ACT}} \tilde{\ell}^2 + A^{\text{kSZ}_\ell \text{kSZ}} + c_8^2 A_{217}^{\text{CIB}} \tilde{\ell}^{\gamma^{\text{CIB}}} + c_9^2 A_{\text{dust}}^{\text{ACTe}} \tilde{\ell}^{-0.7}. \quad (\text{A.12})$$

The extra terms proportional to $\ell^{-0.7}$ represent a residual ‘Galactic cirrus’ contribution [9]. The constants c_4 to c_9 correspond to scalings of the foreground parameters between the Planck and ACT effective frequencies. The calibration factors are $\sigma^{148 \times 148} = \left(y_{148}^{\text{ACTe/s}} \right)^2$, $\sigma^{148 \times 218} = y_{148}^{\text{ACTe/s}} y_{217}^{\text{ACTe/s}}$ and $\sigma^{218 \times 218} = \left(y_{217}^{\text{ACTe/s}} \right)^2$ where $y_{148}^{\text{ACTe/s}}$ and $y_{218}^{\text{ACTe/s}}$ are the map-level calibration parameters for ACTe and ACTs. Beam errors are included in the covariance matrices $N_{bb'\alpha\alpha'}^{II'}$ [9].

A.3 SPT

SPT mapped the CMB anisotropies at 95, 150 and 220 GHz. Following the Planck team only the data reported in [56] is used. The SPT likelihood is

$$L_{\text{SPT}} = \sum_{bb'} \sum_{II'} \left(\frac{s_b^I + f_b^I}{\sigma^I} - d_b^I \right) (N_{bb'}^{-1})^{II'} \left(\frac{s_{b'}^{I'} + f_{b'}^{I'}}{\sigma^{I'}} - d_{b'}^{I'} \right), \quad (\text{A.13})$$

where $I \in \{95 \times 95, 95 \times 150, 95 \times 220, 150 \times 150, 150 \times 220, 220 \times 220\}$ labels the cross-spectra. We use the bandpowers $s_b^I = \sum_\ell W_{b\ell}^I s_\ell^{\text{TT}}$ in the range $2000 \leq \ell \leq 3250$. The foreground bandpowers are $f_b^I = \sum_\ell W_{b\ell}^I f_\ell^I$ where

$$f_\ell^{95 \times 95} = A_{95}^{\text{PS, SPT}} \tilde{\ell}^2 + A^{\text{kSZ}_\ell \text{kSZ}} + c_{10} A^{\text{tSZ}_\ell \text{tSZ}} + c_{11} \tilde{\ell}^{-1.2}, \quad (\text{A.14})$$

$$\begin{aligned} f_\ell^{95 \times 150} &= r_{95 \times 150}^{\text{PS}} \left(A_{95}^{\text{PS, SPT}} A_{150}^{\text{PS, SPT}} \right)^{1/2} \tilde{\ell}^2 + A^{\text{kSZ}_\ell \text{kSZ}} + c_{12} A^{\text{tSZ}_\ell \text{tSZ}} \\ &\quad + (c_{11} c_{13})^{1/2} \tilde{\ell}^{-1.2} - c_{14} (c_{10} A_{143}^{\text{CIB}} A^{\text{tSZ}})^{1/2} \xi^{\text{tSZ} \times \text{CIB}} t_\ell^{\text{tSZ} \times \text{CIB}}, \end{aligned} \quad (\text{A.15})$$

$$\begin{aligned} f_\ell^{95 \times 220} &= r_{95 \times 220}^{\text{PS}} \left(A_{95}^{\text{PS, SPT}} A_{220}^{\text{PS, SPT}} \right)^{1/2} \tilde{\ell}^2 + A^{\text{kSZ}_\ell \text{kSZ}} \\ &\quad + (c_{11} c_{15})^{1/2} \tilde{\ell}^{-1.2} - c_{16} (c_{10} A_{143}^{\text{CIB}} A^{\text{tSZ}})^{1/2} \xi^{\text{tSZ} \times \text{CIB}} t_\ell^{\text{tSZ} \times \text{CIB}}, \end{aligned} \quad (\text{A.16})$$

$$\begin{aligned} f_\ell^{150 \times 150} &= A_{150}^{\text{PS, SPT}} \tilde{\ell}^2 + A^{\text{kSZ}_\ell \text{kSZ}} + c_{17} A^{\text{tSZ}_\ell \text{tSZ}} + c_{14}^2 A_{143}^{\text{CIB}} \tilde{\ell}^{\gamma^{\text{CIB}}} \\ &\quad + c_{13} \tilde{\ell}^{-1.2} - 2c_{14} (c_{17} A_{143}^{\text{CIB}} A^{\text{tSZ}})^{1/2} \xi^{\text{tSZ} \times \text{CIB}} t_\ell^{\text{tSZ} \times \text{CIB}}, \end{aligned} \quad (\text{A.17})$$

$$\begin{aligned} f_\ell^{150 \times 220} &= r_{150 \times 220}^{\text{PS}} \left(A_{150}^{\text{PS, SPT}} A_{220}^{\text{PS, SPT}} \right)^{1/2} \tilde{\ell}^2 + A^{\text{kSZ}_\ell \text{kSZ}} \\ &\quad + c_{14} c_{16} r_{143 \times 217}^{\text{CIB}} (A_{143}^{\text{CIB}} A_{217}^{\text{CIB}})^{1/2} \tilde{\ell}^{\gamma^{\text{CIB}}} + (c_{13} c_{15})^{1/2} \tilde{\ell}^{-1.2} \\ &\quad - c_{16} (c_{17} A_{217}^{\text{CIB}} A^{\text{tSZ}})^{1/2} \xi^{\text{tSZ} \times \text{CIB}} t_\ell^{\text{tSZ} \times \text{CIB}}, \end{aligned} \quad (\text{A.18})$$

$$f_\ell^{220 \times 220} = A_{220}^{\text{PS, SPT}} \tilde{\ell}^2 + A^{\text{kSZ}_\ell \text{kSZ}} + c_{16}^2 A_{217}^{\text{CIB}} \tilde{\ell}^{\gamma^{\text{CIB}}} + c_{15} \tilde{\ell}^{-1.2}. \quad (\text{A.19})$$

The $\ell^{-1.2}$ terms originate from Galactic dust emission [9]. The calibration uncertainties are related to the map-level calibration parameters y_{95}^{SPT} , y_{150}^{SPT} and y_{220}^{SPT} through $\sigma^{95 \times 95} = (y_{95}^{\text{SPT}})^2$, $\sigma^{95 \times 150} = y_{95}^{\text{SPT}} y_{150}^{\text{SPT}}$, $\sigma^{95 \times 220} = y_{95}^{\text{SPT}} y_{220}^{\text{SPT}}$, $\sigma^{150 \times 150} = (y_{150}^{\text{SPT}})^2$, $\sigma^{150 \times 220} = y_{150}^{\text{SPT}} y_{220}^{\text{SPT}}$ and $\sigma^{220 \times 220} = (y_{220}^{\text{SPT}})^2$ [9].

A.4 WiggleZ

The WiggleZ galaxy redshift survey measured the galaxy power spectrum $\mathcal{P}_{\text{gal}}(k)$ using the photometric redshift estimates of 1.7×10^5 galaxies over seven regions of the sky in four redshift bins centred at $z = \{0.22, 0.41, 0.60, 0.78\}$, with a total volume of $\sim 1 \text{ Gpc}^3$. In what follows the index I labels the redshift bin and the index r labels the sky region. To obtain the theoretical galaxy power spectrum at each redshift we use the ‘N-body simulation calibrated without damping’ method recommended by the WiggleZ team [6], so that

$$\mathcal{P}_{\text{gal}}^I(k) \equiv b^2 \frac{\mathcal{P}_{\text{hf}}^{\text{it},I}(k)}{\mathcal{P}_{\mathcal{R}}^{\text{it}}(k)} \frac{\mathcal{P}_{\text{poly}}^{\text{fid},I}(k)}{\mathcal{P}_{\text{hf}}^{\text{fid},I}(k)} \mathcal{P}_{\mathcal{R}}(k). \quad (\text{A.20})$$

Here $\mathcal{P}_{\mathcal{R}}^{\text{it}}(k)$ is a power-law fit in the wavenumber range $0.01 < k < 0.3 \text{ Mpc}^{-1}$ to the PPS recovered at each iteration of the Newton-Raphson minimisation, and $\mathcal{P}_{\text{hf}}^{\text{it},I}$ is the **Halofit** [57] fitting formula for the nonlinear matter power spectrum at redshift I corresponding to $\mathcal{P}_{\mathcal{R}}^{\text{it}}(k)$. Hence on small scales where nonlinear effects are negligible, $\mathcal{P}_{\text{hf}}^{\text{it},I}(k)/\mathcal{P}_{\mathcal{R}}^{\text{it}}(k)$ equals $T^2(k)$, the square of the linear matter transfer function. The power-law fit is used because it is unclear how to apply the **Halofit** formula to matter power spectra with localised features. The factor $\mathcal{P}_{\text{poly}}^{\text{fid},I}(k)/\mathcal{P}_{\text{hf}}^{\text{fid},I}(k)$ accounts for additional nonlinear and redshift space distortion effects specific to WiggleZ, as determined from the **GiggleZ** N-body simulations. The quantity $\mathcal{P}_{\text{hf}}^{\text{fid},I}$ is the **Halofit** nonlinear matter power spectrum at redshift I for the **GiggleZ** fiducial cosmological model, and $\mathcal{P}_{\text{poly}}^{\text{fid},I}$ is a fifth-order polynomial fit to the **GiggleZ** power spectrum at redshift I .

The galaxy power spectrum $\mathcal{P}_{\text{gal}}^I(k)$ is related to d_a^{Ir} , the a^{th} power spectrum measurement in the r^{th} region at the I^{th} redshift, by a convolution with a window function $W_a^{Ir}(k)$ that depends on the WiggleZ survey geometry. As in our previous paper [1] we transform the window function into $\mathcal{W}_a^{Ir}(k) \equiv (\gamma^I)^{-2} W_a^{Ir}(\gamma^I k)$ to account for the fact that the mapping from redshift space to real space depends on the assumed cosmological model. Here the ‘Alcock-Paczynski scaling factor’ γ^I is

$$\gamma^I \equiv \left[\frac{(D_{\text{A}}^I)^2 H_{\text{fid}}^I}{(D_{\text{A,fid}}^I)^2 H^I} \right]^{1/3}, \quad (\text{A.21})$$

where D_{A}^I is the angular diameter distance and H^I is the Hubble parameter, both at the I^{th} redshift, and the subscript ‘fid’ refers to the quantities for the fiducial model assumed by the WiggleZ team. The WiggleZ data points are then

$$\text{d}_a^{Ir} = \int_0^\infty \mathcal{W}_a^{Ir}(k) \mathcal{P}_{\text{gal}}^I(k) \text{d}k + \text{n}_a^{Ir}, \quad (\text{A.22})$$

where n_a^{Ir} is an additive noise term. Using 2.2 and A.20 gives $s_a^{Ir} = \sum_i W_{ai}^{Ir} p_i$. The likelihood function has the Gaussian form

$$L_{\text{WiggleZ}} = \sum_{aa'} \sum_{Ir} (s_a^{Ir} - \text{d}_a^{Ir}) (N_{aa'}^{-1})^{Ir} (s_{a'}^{Ir} - \text{d}_{a'}^{Ir}). \quad (\text{A.23})$$

Note that the different redshift bins and the sky regions are uncorrelated.

A.5 Galaxy clusters

The variance of the matter density contrast smoothed over a scale R using the top-hat filter $F(x) = 3(\sin x - x \cos x)/x^3$ is

$$\sigma_R^2 = \frac{1}{2\pi^2} \int F^2(kR) \mathcal{P}_m(k) k^2 dk. \quad (\text{A.24})$$

Observations of galaxy cluster abundance, when fitted to semi-analytic predictions for the halo mass function, constrain the combination $\sigma_8 \Omega_m^q$ where $q \simeq 0.4$ [64, 65]. In [66] the Planck collaboration compiled the results of 5 recent galaxy cluster experiments and presented them in their table 2 as constraints on the quantity $\Sigma_8 = \sigma_8 (\Omega_m/0.27)^{0.3}$.

The Chandra Cluster Cosmology Project (CCCP) used X-ray observations of 49 nearby ($z < 0.2$) and 37 distant ($0.4 < z < 0.9$) galaxy clusters to obtain $\Sigma_8 = 0.784 \pm 0.027$ [67]. The clusters were first detected by the ROSAT satellite and then reobserved with the Chandra satellite. From 10810 clusters of the optically selected SDSS MaxBCG catalogue, which lie in the range $0.1 < z < 0.3$, Rozo *et al.* found $\Sigma_8 = 0.806 \pm 0.033$ [68]. In the likelihood analyses of the CCCP and MaxBCG data, ω_b and n_s were held fixed at values consistent with the WMAP5 results. In the MaxBCG analysis the hubble parameter was set to $h = 0.7$, while a prior on h derived from Hubble Space Telescope (HST) observations was applied in the CCCP analysis.

A collection of 15 SZ clusters in the range $0.2 < z < 1.4$ detected with the Sunyaev-Zeldovich (SZ) effect by ACT with optical follow-up observations gave $\Sigma_8 = 0.848 \pm 0.032$ [69]. This measurement neglects the uncertainty in the SZ scaling relation parameters, which were held fixed at values taken from a certain gas pressure profile model. The Planck collaboration found $\Sigma_8 = 0.764 \pm 0.025$ using 189 high signal-to-noise clusters from the Planck SZ catalogue with redshifts up to $z = 1$, when the hydrostatic mass bias was allowed to vary between zero and 30%. If the bias was fixed at the best-fit value from numerical simulations of 20% then $\Sigma_8 = 0.78 \pm 0.01$ [66]. A study of 698 clusters at redshift $z < 0.5$ from the REFLEX II X-ray catalogue using X-ray luminosity as a mass proxy derived $\Sigma_8 = 0.80 \pm 0.03$ [70]. It held most of the other cosmological parameters fixed at values consistent with the WMAP9 and Planck CMB results. Using 100 SZ clusters in the range $0.3 < z < 1.4$ identified by SPT (of which 63 had optical velocity dispersion measurements and 16 had X-ray observations from either Chandra or the XMM-Newton satellite), [71] reported $\Sigma_8 = 0.809 \pm 0.036$. Both the ACT and SPT analyses employed priors from Big Bang Nucleosynthesis (BBN) and HST data, while Planck used BBN and Baryonic Acoustic Oscillations (BAO) constraints instead.

The scatter in the Σ_8 measurements is greater than the quoted errors, which indicates the presence of unknown systematic errors. We summarise the measurements as $\Sigma_8 = 0.797 \pm 0.050$ and use this in our work. The likelihood function for galaxy clusters is

$$L_{GC} = \frac{(s - d)^2}{\sigma^2}. \quad (\text{A.25})$$

Here $d = (0.27/\Omega_m)^{0.6} \Sigma_8^2$, σ is the uncertainty in d and $s = \sum_i W_i p_i$, where W_i is derived from Eq.(A.24).

A.6 CFHTLenS

The Canada-France-Hawaii Telescope Lensing Survey (CFHTLenS) covers an area of 154 square degrees in five optical bands. The two-point cosmic shear correlation functions $\xi_+(\vartheta)$ and $\xi_-(\vartheta)$ were estimated from the ellipticity and photometric redshift measurements of 4.2 million galaxies in the redshift range $0.2 < z < 1.3$. Two-point shear statistics are related to the convergence power spectrum $\mathcal{P}_\kappa(\ell)$, which is given by a weighted integral of the matter power spectrum $\mathcal{P}_m(k, z)$ along the line of sight [62, 63]:

$$\mathcal{P}_\kappa(\ell) = \frac{9\Omega_m^2 H_0^4}{4c^4} \int_0^{\chi_H} \frac{g^2(\chi)}{a^2(\chi)} \mathcal{P}_m \left[\frac{\ell}{D_A(\chi)}, z(\chi) \right] d\chi. \quad (\text{A.26})$$

Here

$$\chi(z) = c \int_0^z \frac{dz'}{H(z')} \quad (\text{A.27})$$

is the radial comoving distance of a source at redshift z , χ_H denotes the horizon distance and $a(\chi)$ is the scale factor at a distance χ . The comoving angular diameter distance $D_A(\chi)$ out to a distance χ depends on the curvature of the universe:

$$D_A(\chi) = \begin{cases} cH_0^{-1} \Omega_K^{-1/2} \sinh \left(\Omega_K^{1/2} c^{-1} H_0 \chi \right) & \text{for } \Omega_K > 0 \\ \chi & \text{for } \Omega_K = 0 \\ cH_0^{-1} |\Omega_K|^{-1/2} \sin \left(|\Omega_K|^{1/2} c^{-1} H_0 \chi \right) & \text{for } \Omega_K < 0. \end{cases} \quad (\text{A.28})$$

The lensing efficiency function $g(\chi)$ is defined as

$$g(\chi) = \int_\chi^{\chi_H} \rho[z(\chi')] \frac{dz}{d\chi'} \frac{D_A(\chi' - \chi)}{D_A(\chi')} d\chi', \quad (\text{A.29})$$

where $\rho(z)$ is the redshift distribution of the source galaxies normalised to unity,

$$\int_0^\infty \rho(z) dz = 1. \quad (\text{A.30})$$

The shear correlation functions are Hankel transforms of the convergence power spectrum,

$$\xi_{+/-}(\vartheta) = \frac{1}{2\pi} \int_0^\infty J_{0/4}(\ell\vartheta) \mathcal{P}_\kappa(\ell) \ell d\ell, \quad (\text{A.31})$$

where ξ_+ and ξ_- correspond to J_0 and J_4 respectively, Bessel functions of the first kind of order 0 and 4. Using the substitution $k = \ell/D_A(\chi')$ this can be rewritten as

$$\xi_{+/-}(\vartheta) = \int_0^\infty \mathcal{K}_{+/-}(\boldsymbol{\theta}, \vartheta, k) \mathcal{P}_{\mathcal{R}}(k) dk. \quad (\text{A.32})$$

Here the integral kernels are

$$\mathcal{K}_{+/-}(\boldsymbol{\theta}, \vartheta, k) = \frac{9\Omega_m^2 H_0^4}{8\pi c^4} \int_0^{\chi_H} \frac{D_A^2(\chi) g^2(\chi)}{a^2(\chi)} J_{0/4}[k D_A(\chi) \vartheta] \frac{\mathcal{P}_{\text{hf}}^{\text{it}}[k, z(\chi)]}{\mathcal{P}_{\mathcal{R}}^{\text{it}}(k)} k d\chi, \quad (\text{A.33})$$

where $\mathcal{P}_{\mathcal{R}}^{\text{it}}(k)$ is a power-law fit in the wavenumber range $0.01 < k < 0.3 \text{ Mpc}^{-1}$ to the PPS recovered at each iteration of the Newton-Raphson minimisation, and $\mathcal{P}_{\text{hf}}^{\text{it}}(k, z)$ is the

Halofit nonlinear matter power spectrum corresponding to $\mathcal{P}_{\mathcal{R}}^{\text{it}}(k)$. We exclude angular scales for which nonlinear evolution alters the shear correlation functions by more than 20%. Thus ξ_+ and ξ_- data points are retained for $\vartheta > 12$ arc min and $\vartheta > 53$ arc min respectively, as ξ_- is more sensitive to nonlinear effects than ξ_+ .

Denoting the observed values and the theoretical predictions of $\xi_{+/-}(\vartheta_a)$ by d_a^μ and s_a^μ respectively, the likelihood function is

$$L_{\text{CFHTLenS}} = \sum_{aa'} \sum_{\mu\nu} (s_a^\mu - d_a^\mu) (N_{aa'}^{-1})^{\mu\nu} (s_{a'}^\nu - d_{a'}^\nu). \quad (\text{A.34})$$

Here a and a' label the angular scale while μ and ν stand for the ‘+’ and ‘−’ components. The covariance matrix $N_{aa'}^{\mu\nu}$ was calculated for a fiducial model.

A.7 Lyman- α data

VHS [8] used Lyman- α forest observations by Croft [58] and LUQAS (Large Sample of UVES QSO Absorption Spectra) [59] to estimate the linear matter power spectrum on scales $0.3 \, h/\text{Mpc} \lesssim k \lesssim 3 \, h/\text{Mpc}$. The LUQAS sample consists of 27 high-resolution quasar spectra taken by the UVES spectrograph on the Very Large Telescope. The Croft sample comprises 30 high-resolution and 23 low-resolution spectra obtained using the HIRES and LRIS instruments of the Keck observatory. The mean absorption redshift of the Croft and LUQAS samples is $z_{\text{Croft}} \simeq 2.72$ and $z_{\text{LUQAS}} \simeq 2.25$. VHS employed the so-called ‘effective bias’ method [60] calibrated by a suite of hydrodynamical simulations to infer the matter power spectrum from the transmitted flux power spectrum of the two datasets. The VHS results were subsequently incorporated into the CosmoMC module `lya.f90` [61].

The Lyman- α likelihood is $L_{\text{Ly}\alpha} \equiv L_{\text{Croft}} + L_{\text{LUQAS}}$ where

$$L_{\text{Croft/LUQAS}} = \sum_a \frac{\left(s_a / Q_\Omega^{\text{Croft/LUQAS}} - A d_a \right)^2}{\sigma_a^2}. \quad (\text{A.35})$$

Here s_a and d_a are the theoretical and measured matter power spectrum data points respectively, σ_a^2 is the variance of the uncorrelated measurement errors and $A = 1 \pm 0.29$ is the overall calibration error of the effective bias method. The latter originates mainly from uncertainties in the numerical simulations, the effective optical depth, the mean temperature of the intergalactic medium and the slope of the temperature-density relation. The factor

$$Q_\Omega^{\text{Croft/LUQAS}} = \left[\frac{2.4}{1 + 1.4 \Omega_{\text{m}}^{0.6} (z_{\text{Croft/LUQAS}})} \right]^2 \quad (\text{A.36})$$

accounts for the dependence of the inferred matter power spectrum on the matter density Ω_{m} at the redshift of the Lyman- α data.

A.8 BICEP2/Keck Array

The BICEP2/Keck Array collaboration employed the Hamimeche-Lewis approximation [79] to construct the likelihood function, which features a vector of transformed bandpowers:

$$\begin{pmatrix} X_b^{EE} \\ X_b^{BB} \\ X_b^{EB} \end{pmatrix} = \text{vecp} \left[D_{\text{fid},b}^{1/2} \mathcal{G}(U_b) D_{\text{fid},b}^{1/2} \right]. \quad (\text{A.37})$$

Here $\mathbf{U}_b = \mathbf{S}_b^{-1/2} \mathbf{D}_b \mathbf{S}_b^{-1/2}$ and

$$\mathbf{D}_b = \begin{pmatrix} d_b^{EE} & d_b^{EB} \\ d_b^{EB} & d_b^{BB} \end{pmatrix}, \quad \mathbf{S}_b = \begin{pmatrix} s_b^{EE} & s_b^{EB} \\ s_b^{EB} & s_b^{BB} \end{pmatrix}, \quad \mathbf{D}_{\text{fid},b} = \begin{pmatrix} d_{\text{fid},b}^{EE} & d_{\text{fid},b}^{EB} \\ d_{\text{fid},b}^{EB} & d_{\text{fid},b}^{BB} \end{pmatrix}, \quad (\text{A.38})$$

are matrices formed from the measured, theoretical and fiducial bandpowers respectively. The operator vecp stacks the distinct elements of a symmetric matrix to produce a vector. The action of the operator \mathcal{G} on a matrix \mathbf{U} is

$$[\mathcal{G}(\mathbf{U})]_{ij} = \begin{cases} g(U_{ii}) \delta_{ij} & \text{for } \mathbf{U} \text{ diagonal,} \\ [\mathbf{O}g(\mathbf{\Lambda})\mathbf{O}^t]_{ij} & \text{for } \mathbf{U} \text{ symmetric positive-definite,} \end{cases} \quad (\text{A.39})$$

where $\mathbf{\Lambda} = \mathbf{O}^t \mathbf{U} \mathbf{O}$ results from the diagonalisation of \mathbf{U} (\mathbf{O} is orthogonal) and

$$g(x) = \begin{cases} \sqrt{2(x - \ln x - 1)} & \text{for } x > 1, \\ -\sqrt{2(x - \ln x - 1)} & \text{for } x < 1. \end{cases} \quad (\text{A.40})$$

The BICEP2 likelihood function is then

$$L_{\text{BICEP}} = \sum_{bb'} \sum_{II'} X_b^I (N_{bb'}^{-1})^{II'} X_{b'}^{I'}, \quad (\text{A.41})$$

where $I \in \{\text{EE}, \text{BB}, \text{EB}\}$, the index b labels the bandpowers and the covariance matrix $N_{bb'}^{II'}$ was calculated for a fiducial model.

The spectrum of the polarised dust foreground can be written as

$$f_\ell^{XX} = \frac{A^{XX}}{2} \tilde{\ell} (\tilde{\ell} + 1) \tilde{\ell}^{\alpha_{XX}}, \quad (\text{A.42})$$

where $XX \in \{\text{EE}, \text{BB}\}$ and $\tilde{\ell} = \ell/80$. Following [77] we set $\alpha_{XX} = -2.42$ and $A^{BB}/A^{EE} = 0.53$. The predicted BICEP2/Keck Array bandpowers are

$$s_b^{EE} = \sum_{\ell} W_{b\ell}^{EE} (s_\ell^{EE} + f_\ell^{EE}) + b_b^{EE}, \quad (\text{A.43})$$

$$s_b^{EB} = b_b^{EB}, \quad (\text{A.44})$$

$$s_b^{BB} = \sum_{\ell} W_{b\ell}^{BB} (s_\ell^{BB} + f_\ell^{BB}) + b_b^{BB}. \quad (\text{A.45})$$

Here $W_{b\ell}^{XX}$ are the bandpower window functions and b_b^I are noise bias terms arising from instrumental noise and E to B leakage.

The off-diagonal elements of \mathbf{U}_b are subdominant so that

$$\mathcal{G}(\mathbf{U}_b) \simeq \text{diag} \left(g(d_b^{EE}/s_b^{EE}), g(d_b^{BB}/s_b^{BB}) \right). \quad (\text{A.46})$$

This approximation has little effect on the reconstructed spectra yet allows us to calculate L_{BICEP} and its derivatives analytically. We use only the lowest 5 bandpowers as higher ones are dominated by the contribution from EE lensing.

A.9 WMAP9 polarisation

The pixel-based WMAP9 polarisation likelihood L_{WP} covers $\ell \leq 23$ and uses the WMAP9 polarisation maps at 33, 41 and 61 GHz. The Planck team updated the temperature map used in constructing the likelihood to the Planck Commander map. Our handling of this data set is the same as in our previous paper [1].

B Error analysis

When generalised to include perturbative nonlinear effects Eq.(2.1) becomes

$$\begin{aligned} d_a^{(\mathbb{Z})} = & c_a^{(\mathbb{Z})}(\boldsymbol{\theta}) + \int_0^\infty \mathcal{K}_a^{(\mathbb{Z})}(\boldsymbol{\theta}, k) \mathcal{P}_{\mathcal{R}}(k) dk \\ & + \int_0^\infty \int_0^\infty \mathcal{K}_a^{(\mathbb{Z})}(\boldsymbol{\theta}, k_1, k_2) \mathcal{P}_{\mathcal{R}}(k_1) \mathcal{P}_{\mathcal{R}}(k_2) dk_1 dk_2 + n_a^{(\mathbb{Z})}, \end{aligned} \quad (\text{B.1})$$

which is valid in the mildly nonlinear regime. Using the expansion Eq.(2.2) gives

$$d_a^{(\mathbb{Z})} = c_a^{(\mathbb{Z})}(\boldsymbol{\theta}) + \sum_i W_{ai}^{(\mathbb{Z})}(\boldsymbol{\theta}) p_i + \frac{1}{2} \sum_{ij} S_{aij}^{(\mathbb{Z})}(\boldsymbol{\theta}) p_i p_j + n_a^{(\mathbb{Z})}, \quad (\text{B.2})$$

where

$$S_{aij}^{(\mathbb{Z})}(\boldsymbol{\theta}) = \int_{k_i}^{k_{i+1}} \int_{k_j}^{k_{j+1}} \mathcal{K}_a^{(\mathbb{Z})}(\boldsymbol{\theta}, k_1, k_2) dk_1 dk_2. \quad (\text{B.3})$$

We emphasise that the additional nonlinear terms are *not* used elsewhere in this paper but are included here for completeness.

Any deconvolution method for recovering the PPS defines a transfer function \mathcal{T} which gives the relationship of the estimate $\hat{\mathbf{y}}$ to the true PPS \mathbf{y}_{tru} . It depends on the true background parameters $\boldsymbol{\theta}_{\text{tru}}$, the estimated background parameters $\hat{\boldsymbol{\theta}}$ and the noise in the data \mathbf{n} so that

$$\hat{\mathbf{y}}(\mathbf{d}, \hat{\boldsymbol{\theta}}) = \mathcal{T}(\mathbf{y}_{\text{tru}}, \boldsymbol{\theta}_{\text{tru}}, \hat{\boldsymbol{\theta}}, \mathbf{n}). \quad (\text{B.4})$$

Performing a Taylor expansion of \mathcal{T} about a fiducial PPS \mathbf{y}_{fid} close to \mathbf{y}_{tru} yields

$$\begin{aligned} \hat{y}_i(\mathbf{d}, \hat{\boldsymbol{\theta}}) = & \mathcal{T}_i(\mathbf{y}_{\text{tru}}, \boldsymbol{\theta}_{\text{tru}}, \boldsymbol{\theta}_{\text{tru}}, \mathbf{0}) + \sum_j R_{ij} \Delta y_j + \frac{1}{2} \sum_{j,k} Y_{ijk} \Delta y_j \Delta y_k \\ & + \sum_{\mathbb{Z}, a} M_{ia}^{(\mathbb{Z})} n_a^{(\mathbb{Z})} + \sum_{\alpha} M_{i\alpha} u_{\alpha} + \sum_{\mathbb{Z}, j, a} Z_{ija}^{(\mathbb{Z})} \Delta y_j n_a^{(\mathbb{Z})} + \sum_{j, \alpha} Z_{ij\alpha} \Delta y_j u_{\alpha} \\ & + \frac{1}{2} \sum_{\mathbb{Z}, \mathbb{Z}', a, b} X_{iab}^{(\mathbb{Z}\mathbb{Z}')} n_a^{(\mathbb{Z})} n_b^{(\mathbb{Z}')} + \sum_{\mathbb{Z}, a, \alpha} X_{ia\alpha}^{(\mathbb{Z})} n_a^{(\mathbb{Z})} u_{\alpha} + \frac{1}{2} \sum_{\alpha, \beta} X_{i\alpha\beta} u_{\alpha} u_{\beta} + \dots \end{aligned} \quad (\text{B.5})$$

Here $\Delta y_i \equiv y_{\text{tru}|i} - y_{\text{fid}|i}$,

$$\begin{aligned} M_{ia}^{(\mathbb{Z})} & \equiv \left. \frac{\partial \hat{y}_i}{\partial d_a^{(\mathbb{Z})}} \right|_{\hat{\mathbf{d}}_{\text{fid}}, \boldsymbol{\theta}_{\text{tru}}}, & M_{i\alpha} & \equiv \left. \frac{\partial \hat{y}_i}{\partial \theta_{\alpha}} \right|_{\hat{\mathbf{d}}_{\text{fid}}, \boldsymbol{\theta}_{\text{tru}}}, \\ X_{iab}^{(\mathbb{Z}\mathbb{Z}')} & \equiv \left. \frac{\partial^2 \hat{y}_i}{\partial d_a^{(\mathbb{Z})} \partial d_b^{(\mathbb{Z}')}} \right|_{\hat{\mathbf{d}}_{\text{fid}}, \boldsymbol{\theta}_{\text{tru}}}, & X_{ia\alpha}^{(\mathbb{Z})} & \equiv \left. \frac{\partial^2 \hat{y}_i}{\partial d_a^{(\mathbb{Z})} \partial \theta_{\alpha}} \right|_{\hat{\mathbf{d}}_{\text{fid}}, \boldsymbol{\theta}_{\text{tru}}}, & X_{i\alpha\beta} & \equiv \left. \frac{\partial^2 \hat{y}_i}{\partial \theta_{\alpha} \partial \theta_{\beta}} \right|_{\hat{\mathbf{d}}_{\text{fid}}, \boldsymbol{\theta}_{\text{tru}}}, \end{aligned}$$

where $\hat{\mathbf{d}}_{\text{fid}}$ denotes collectively the datasets estimated from \mathbf{y}_{fid} , i.e.

$$\hat{d}_{\text{fid}|a}^{(\mathbb{Z})} = c_a^{(\mathbb{Z})}(\boldsymbol{\theta}_{\text{tru}}) + \sum_i W_{ai}^{(\mathbb{Z})}(\boldsymbol{\theta}_{\text{tru}}) p_{\text{fid}|i} + \frac{1}{2} \sum_{ij} S_{aij}^{(\mathbb{Z})}(\boldsymbol{\theta}_{\text{tru}}) p_{\text{fid}|i} p_{\text{fid}|j}, \quad (\text{B.6})$$

and

$$R_{ij} \equiv \sum_{\mathbb{Z},a} M_{ia}^{(\mathbb{Z})} W_{aj}^{(\mathbb{Z})} (\boldsymbol{\theta}_{\text{tru}}) p_j + \sum_{\mathbb{Z},a,k} M_{ia}^{(\mathbb{Z})} S_{ajk}^{(\mathbb{Z})} (\boldsymbol{\theta}_{\text{tru}}) p_j p_k, \quad (\text{B.7})$$

$$\begin{aligned} Y_{ijk} \equiv & \sum_{\mathbb{Z},\mathbb{Z}',a,b} X_{iab}^{(\mathbb{Z}\mathbb{Z}')} W_{aj}^{(\mathbb{Z})} (\boldsymbol{\theta}_{\text{tru}}) W_{bk}^{(\mathbb{Z}')} (\boldsymbol{\theta}_{\text{tru}}) p_j p_k + \sum_{\mathbb{Z},a} M_{ia}^{(\mathbb{Z})} S_{ajk}^{(\mathbb{Z})} (\boldsymbol{\theta}_{\text{tru}}) p_j p_k, \\ & + \sum_{\mathbb{Z},\mathbb{Z}',a,b,l} X_{iab}^{(\mathbb{Z}\mathbb{Z}')} S_{ajl}^{(\mathbb{Z})} (\boldsymbol{\theta}_{\text{tru}}) W_{bk}^{(\mathbb{Z}')} (\boldsymbol{\theta}_{\text{tru}}) p_j p_k p_l + \delta_{jk} \sum_{\mathbb{Z},a} M_{ia}^{(\mathbb{Z})} W_{aj}^{(\mathbb{Z})} (\boldsymbol{\theta}_{\text{tru}}) p_k, \\ & + \sum_{\mathbb{Z},\mathbb{Z}',a,b,l} X_{iab}^{(\mathbb{Z}\mathbb{Z}')} W_{aj}^{(\mathbb{Z})} (\boldsymbol{\theta}_{\text{tru}}) S_{bkl}^{(\mathbb{Z}')} (\boldsymbol{\theta}_{\text{tru}}) p_j p_k p_l + \delta_{jk} \sum_{\mathbb{Z},a,l} M_{ia}^{(\mathbb{Z})} S_{ajl}^{(\mathbb{Z})} (\boldsymbol{\theta}_{\text{tru}}) p_k p_l, \\ & + \sum_{\mathbb{Z},\mathbb{Z}',a,b,l,m} X_{iab}^{(\mathbb{Z}\mathbb{Z}')} S_{ajl}^{(\mathbb{Z})} (\boldsymbol{\theta}_{\text{tru}}) S_{bkm}^{(\mathbb{Z}')} (\boldsymbol{\theta}_{\text{tru}}) p_j p_k p_j p_m, \end{aligned} \quad (\text{B.8})$$

$$Z_{ija}^{(\mathbb{Z})} \equiv \sum_{\mathbb{Z}',b} X_{iab}^{(\mathbb{Z}\mathbb{Z}')} W_{bj}^{(\mathbb{Z}')} (\boldsymbol{\theta}_{\text{tru}}) p_j + \sum_{\mathbb{Z}',b,k} X_{iab}^{(\mathbb{Z}\mathbb{Z}')} S_{bjk}^{(\mathbb{Z}')} (\boldsymbol{\theta}_{\text{tru}}) p_j p_k, \quad (\text{B.9})$$

$$Z_{ij\alpha} \equiv \sum_{\mathbb{Z},a} X_{ia\alpha}^{(\mathbb{Z})} W_{aj}^{(\mathbb{Z})} (\boldsymbol{\theta}_{\text{tru}}) p_j + \sum_{\mathbb{Z},a,k} X_{ia\alpha}^{(\mathbb{Z})} S_{ajk}^{(\mathbb{Z})} (\boldsymbol{\theta}_{\text{tru}}) p_j p_k. \quad (\text{B.10})$$

These matrices characterise the inversion and are discussed in more detail in [1]. In particular the first-order resolution matrix \mathbf{R} describes the linear mapping from \mathbf{y}_{tru} to $\hat{\mathbf{y}}$. The closer \mathbf{R} is to the identity matrix \mathbf{I} , the better the resolution and the lower the bias of the inversion method. For Tikhonov regularisation $\sum_j R_{ij} \simeq 1$ for all i so that the estimated PPS is correctly scaled. The second-order resolution matrix \mathbf{Y} details a quadratic mapping of \mathbf{y}_{tru} to $\hat{\mathbf{y}}$ and should vanish in order to minimise the bias. For Tikhonov regularisation analytic expressions for these inversion matrices can be derived as in [1]:

$$M_{ia}^{(\mathbb{Z})} = - \sum_j A_{ij}^{-1} B_{ja}^{(\mathbb{Z})}, \quad M_{i\alpha} = - \sum_j A_{ij}^{-1} B_{j\alpha}, \quad (\text{B.11})$$

$$X_{iab}^{(\mathbb{Z}\mathbb{Z}')} = - \sum_{j,k,l} A_{ij}^{-1} C_{jkl} M_{ka}^{(\mathbb{Z})} M_{lb}^{(\mathbb{Z}')} - \sum_{j,k} A_{ij}^{-1} E_{jka}^{(\mathbb{Z})} M_{kb}^{(\mathbb{Z}')} - \sum_{j,k} A_{ij}^{-1} E_{jkb}^{(\mathbb{Z}')} M_{ka}^{(\mathbb{Z})} - \sum_j A_{ij}^{-1} D_{jab}^{(\mathbb{Z}\mathbb{Z}')}, \quad (\text{B.12})$$

$$X_{ia\alpha}^{(\mathbb{Z})} = - \sum_{j,k,l} A_{ij}^{-1} C_{jkl} M_{ka}^{(\mathbb{Z})} M_{l\alpha} - \sum_{j,k} A_{ij}^{-1} E_{jka}^{(\mathbb{Z})} M_{k\alpha} - \sum_{j,k} A_{ij}^{-1} E_{jk\alpha} M_{ka}^{(\mathbb{Z})} - \sum_j A_{ij}^{-1} D_{ja\alpha}^{(\mathbb{Z})}. \quad (\text{B.13})$$

$$X_{i\alpha\beta} = - \sum_{j,k,l} A_{ij}^{-1} C_{jkl} M_{k\alpha} M_{l\beta} - \sum_{j,k} A_{ij}^{-1} E_{jka} M_{k\beta} - \sum_{j,k} A_{ij}^{-1} E_{jk\beta} M_{k\alpha} - \sum_j A_{ij}^{-1} D_{j\alpha\beta}, \quad (\text{B.14})$$

$$\begin{aligned} A_{ij} &\equiv \left. \frac{\partial^2 Q}{\partial y_i \partial y_j} \right|_{\hat{\mathbf{y}}_{\text{fid}}, \hat{\mathbf{d}}_{\text{fid}}, \boldsymbol{\theta}_{\text{tru}}}, & B_{ia}^{(\mathbb{Z})} &\equiv \left. \frac{\partial^2 Q}{\partial y_i \partial d_a^{(\mathbb{Z})}} \right|_{\hat{\mathbf{y}}_{\text{fid}}, \hat{\mathbf{d}}_{\text{fid}}, \boldsymbol{\theta}_{\text{tru}}}, & B_{i\alpha} &\equiv \left. \frac{\partial^2 Q}{\partial y_i \partial \theta_\alpha} \right|_{\hat{\mathbf{y}}_{\text{fid}}, \hat{\mathbf{d}}_{\text{fid}}, \boldsymbol{\theta}_{\text{tru}}} \\ C_{ijk} &\equiv \left. \frac{\partial^3 Q}{\partial y_i \partial y_j \partial y_k} \right|_{\hat{\mathbf{y}}_{\text{fid}}, \hat{\mathbf{d}}_{\text{fid}}, \boldsymbol{\theta}_{\text{tru}}}, & D_{iab}^{(\mathbb{Z}\mathbb{Z}')} &\equiv \left. \frac{\partial^3 Q}{\partial y_i \partial d_a^{(\mathbb{Z})} \partial d_b^{(\mathbb{Z}')}} \right|_{\hat{\mathbf{y}}_{\text{fid}}, \hat{\mathbf{d}}_{\text{fid}}, \boldsymbol{\theta}_{\text{tru}}}, & D_{ia\alpha}^{(\mathbb{Z})} &\equiv \left. \frac{\partial^3 Q}{\partial y_i \partial d_a^{(\mathbb{Z})} \partial \theta_\alpha} \right|_{\hat{\mathbf{y}}_{\text{fid}}, \hat{\mathbf{d}}_{\text{fid}}, \boldsymbol{\theta}_{\text{tru}}} \\ D_{i\alpha\beta} &\equiv \left. \frac{\partial^3 Q}{\partial y_i \partial \theta_\alpha \partial \theta_\beta} \right|_{\hat{\mathbf{y}}_{\text{fid}}, \hat{\mathbf{d}}_{\text{fid}}, \boldsymbol{\theta}_{\text{tru}}}, & E_{ija}^{(\mathbb{Z})} &\equiv \left. \frac{\partial^3 Q}{\partial y_i \partial y_j \partial d_a^{(\mathbb{Z})}} \right|_{\hat{\mathbf{y}}_{\text{fid}}, \hat{\mathbf{d}}_{\text{fid}}, \boldsymbol{\theta}_{\text{tru}}}, & E_{ij\alpha} &\equiv \left. \frac{\partial^3 Q}{\partial y_i \partial y_j \partial \theta_\alpha} \right|_{\hat{\mathbf{y}}_{\text{fid}}, \hat{\mathbf{d}}_{\text{fid}}, \boldsymbol{\theta}_{\text{tru}}}. \end{aligned} \quad (\text{B.15})$$

Here the derivatives are evaluated at $\hat{\mathbf{y}}_{\text{fid}} \equiv \hat{\mathbf{y}}(\hat{\mathbf{d}}_{\text{fid}}, \boldsymbol{\theta}_{\text{tru}})$. The functions

$$R(k_0, k) \equiv \sum_{i,j} R_{ij} \phi_i(k_0) \phi_j(k), \quad (\text{B.16})$$

$$Y(k_0, k_1, k_2) \equiv \sum_{i,j,k} Y_{ijk} \phi_i(k_0) \phi_j(k_1) \phi_k(k_2), \quad (\text{B.17})$$

known as resolution kernels are more suitable for plotting than the resolution matrices. The first-order kernel $R(k_0, k)$ describes the extent to which the estimated PPS is a smoothed version of the true PPS. For fixed k_0 it is a sharply peaked function of k (ideally centred at $k = k_0$) which represents the wavenumber range over which the true PPS is smoothed.

Features in the true PPS $\mathcal{P}_{\mathcal{R}}(k)$ much broader than the resolution kernel $R(k_0, k)$ are recovered well by the estimated PPS $\hat{\mathcal{P}}_{\mathcal{R}}(k_0)$, while features much narrower are smoothed out. The resolution kernels for some chosen values of the target wavenumber k_0 are displayed in Fig. 17. Since the resolution kernels depend on both the integral kernels $\mathcal{K}_a^{(\mathbb{Z})}$ and the error in the data, the greatest resolution is attained on intermediate scales where the cosmic variance and noise in the data is minimised. A clear pattern is that the resolution is better at wavenumbers corresponding to the 7 peaks of the CMB TT spectrum observed by Planck than the troughs. This is because the TT integral kernels are narrower at the acoustic peaks than the troughs. There is a loss of resolution at $k \simeq 0.4 \text{ Mpc}^{-1}$ between the lower wavenumbers covered by the CMB and WiggleZ datasets and the higher wavenumbers covered by the VHS Lyman- α data. Although this gap is spanned by the CFHTLenS weak lensing data it has comparatively poor resolution as it is sparser and noisier than the other datasets.

To measure the resolution we use the width of the resolution kernels, taken to be the quantity $\ln(k_{75}/k_{25})$, the logarithmic wavenumber interval between the 25th and 75th percentiles of the area underneath the absolute value of the resolution kernel. In Fig. 18 the kernel width is plotted against the location of the kernel, defined as the wavenumber of the 50th percentile k_{50} . The greater resolution at the acoustic peaks and the increase in resolution caused by the addition of extra datasets can clearly be seen.

Using Eq.(B.5) the total frequentist covariance matrix Σ of the estimated PPS is

$$\Sigma \equiv \langle (\hat{\mathbf{y}} - \langle \hat{\mathbf{y}} \rangle) (\hat{\mathbf{y}} - \langle \hat{\mathbf{y}} \rangle)^T \rangle = \Sigma_{\text{F}} + \Sigma_{\text{P}} + \dots, \quad (\text{B.18})$$

$$\Sigma_{\text{F}|ij} \equiv \sum_{\mathbb{Z}, a, b} M_{ia}^{(\mathbb{Z})} N_{ab}^{(\mathbb{Z})} M_{jb}^{(\mathbb{Z})}, \quad (\text{B.19})$$

$$\Sigma_{\text{P}|ij} \equiv M_{i\alpha} U_{\alpha\beta} M_{j\beta}, \quad (\text{B.20})$$

where the angled brackets denote the average over an ensemble of spectra estimated from repeated identical independent measurements of the data and the background parameters. Thus to first order Σ is the sum of Σ_{F} which arises from the data noise and Σ_{P} which arises from errors in the background parameters.

Tikhonov regularisation has a natural Bayesian interpretation as a two-stage hierarchical Bayes model with a hyperparameter $\tilde{\lambda}$, as discussed in [1]. The maximum *a posteriori* estimate that maximises the posterior distribution of the PPS given the data $P(\mathbf{y}|\mathbf{d})$ coincides with $\hat{\mathbf{y}}$ when the prior distributions of $\tilde{\lambda}$ and $\boldsymbol{\theta}$ are $P(\tilde{\lambda}) = \delta(\tilde{\lambda} - \lambda)$ and $P(\boldsymbol{\theta}) = \delta(\boldsymbol{\theta} - \hat{\boldsymbol{\theta}})$.

The Bayesian covariance matrix Π which describes the shape of $P(\mathbf{y}|\mathbf{d})$ is then given by

$$\Pi_{ij}^{-1} \equiv \frac{1}{2} \frac{\partial^2 Q(\mathbf{y}, \mathbf{d}, \hat{\boldsymbol{\theta}}, \lambda)}{\partial y_i \partial y_j} \bigg|_{\hat{\mathbf{y}}}. \quad (\text{B.21})$$

As the regularisation parameter λ decreases, each element of the recovered PPS is effectively dependent on fewer data points. Mathematically, each row of the matrices $M_{ia}^{(\mathbb{Z})}$ becomes a narrower and more sharply peaked function of the index a . This means that the resolution kernels also become narrower, but the noise artifact term $\sum_{\mathbb{Z},a} M_{ia}^{(\mathbb{Z})} n_a^{(\mathbb{Z})}$ in Eq.(B.5) becomes more significant as the noise vectors $n_a^{(\mathbb{Z})}$ are less averaged out. Thus there is an unavoidable trade-off between the resolution and the variance of the recovered PPS.

This can be seen in Fig. 19 in which two measures of resolution quality (kernel width and offset) are plotted against the reconstruction error. The error is computed from the frequentist covariance matrix Σ_F averaged over $5 \times 10^{-3} \leq k \leq 0.25 \text{ Mpc}^{-1}$. The kernel width is defined as in Fig. 18, but now averaged over the kernels $R(k_0, k)$ with $5 \times 10^{-3} \leq k_0 \leq 0.25 \text{ Mpc}^{-1}$. The offset of the kernel $R(k_0, k)$ is defined as the quantity $|k_{50} - k_0|/k_0$. The offset is averaged over the kernels $R(k_0, k)$ with $3.5 \times 10^{-4} \leq k_0 \leq 1.9 \text{ Mpc}^{-1}$.

The trade-off curves in Fig. 19 are shaped like the letter L. The corner of the curves represents the optimum compromise between resolution and variance. The regularisation parameter values $\lambda = 400$ and $\lambda = 20000$ used in our analysis are close to the corner of the curves and are thus satisfactory according to this criterion.

The results above can be generalised to include a tensor PPS simply by replacing \mathbf{p} with \mathbf{P} and \mathbf{y} with \mathbf{Y} . The $2N_k \times 2N_k$ first-order resolution matrix then has four components, each of size $N_k \times N_k$,

$$\mathbf{R} = \begin{pmatrix} \mathbf{R}_{ss} & \mathbf{R}_{ts} \\ \mathbf{R}_{st} & \mathbf{R}_{tt} \end{pmatrix}. \quad (\text{B.22})$$

Here \mathbf{R}_{ss} characterises the linear mapping from \mathbf{y}_{tru} to $\hat{\mathbf{y}}$, \mathbf{R}_{tt} characterises the mapping from \mathbf{z}_{tru} to $\hat{\mathbf{z}}$, \mathbf{R}_{ts} describes an undesirable linear mapping from \mathbf{z}_{tru} to $\hat{\mathbf{y}}$ and \mathbf{R}_{st} describes an undesirable mapping from \mathbf{y}_{tru} to $\hat{\mathbf{z}}$. Ideally \mathbf{R}_{ss} and \mathbf{R}_{tt} should equal \mathbf{I} while \mathbf{R}_{ts} and \mathbf{R}_{st} should vanish.

A selection of scalar and tensor resolution kernels are shown in Fig. 20 for the joint reconstruction from data combination V. The Planck and WMAP-9 polarisation measurements contribute to the resolution of the tensor reconstruction at $k \simeq 4 \times 10^{-4} \text{ Mpc}^{-1}$ but the greatest resolution is attained at $k \simeq 0.01 \text{ Mpc}^{-1}$ due to the BICEP2/Keck Array data. As expected the tensor resolution is much lower than the scalar resolution at this scale because B-mode observations are relatively immature. The tensor resolution kernels exhibit a series of subsidiary peaks to the right of the main peak for high k_0 . This is because the tensor EE and BB integral kernels have a oscillatory decaying envelope for large ℓ , unlike the scalar integral kernels [12]. The scalar and tensor resolution kernel widths are shown as a function of the kernel location in Fig. 21, where it can be seen that the tensor reconstruction at $k \simeq 0.01 \text{ Mpc}^{-1}$ (corresponding to $\ell \simeq 110$) has a similar resolution to the scalar reconstruction at $k \simeq 4 \times 10^{-3} \text{ Mpc}^{-1}$ (equivalent to $\ell \simeq 50$).

The joint frequentist covariance matrix is

$$\Sigma = \langle (\hat{\mathbf{Y}} - \langle \hat{\mathbf{Y}} \rangle) (\hat{\mathbf{Y}} - \langle \hat{\mathbf{Y}} \rangle)^T \rangle = \begin{pmatrix} \Sigma_{ss} & \Sigma_{ts} \\ \Sigma_{ts}^T & \Sigma_{tt} \end{pmatrix}, \quad (\text{B.23})$$

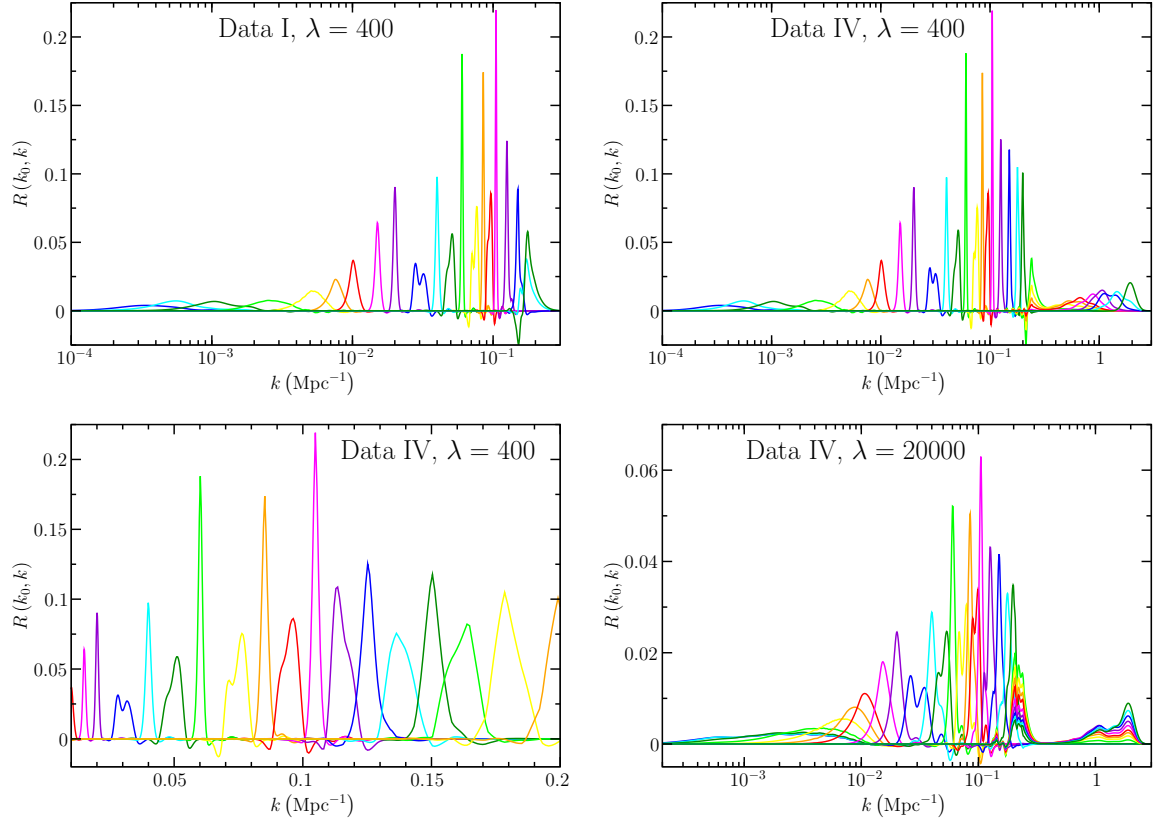


Figure 17. Top left: First-order resolution kernels $R(k_0, k)$ for the Planck and WMAP-9 polarisation data (combination I) with $\lambda = 400$. The kernels are shown for $k_0 = 10^{-4}, 5 \times 10^{-4}, 10^{-3}, 2.5 \times 10^{-3}, 5 \times 10^{-3}, 7.5 \times 10^{-3}, 0.01, 0.015, 0.02, 0.03, 0.04, 0.05, 0.06, 0.075, 0.085, 0.095, 0.105, 0.125, 0.15, 0.18, 0.2 \text{ Mpc}^{-1}$. Top right: Resolution kernels for the Planck, WMAP-9 polarisation, ACT, SPT, WiggleZ, galaxy clustering, CFTHLenS and Lyman- α data (combination IV) with $\lambda = 400$. The k_0 values are the same as in the top left panel, plus $k_0 = 0.3, 0.4, 0.5, 0.6, 0.8, 1, 1.25, 1.5, 2.0 \text{ Mpc}^{-1}$. Bottom left: Same as the top left panel, but for $k_0 = 0.01, 0.015, 0.02, 0.03, 0.04, 0.05, 0.06, 0.075, 0.085, 0.095, 0.105, 0.115, 0.125, 0.138, 0.15, 0.162, 0.18, 0.2 \text{ Mpc}^{-1}$. Bottom right: Same as the top right panel, but with $\lambda = 20000$.

where Σ_{ss} is the covariance of $\hat{\mathbf{y}}$, Σ_{tt} is the covariance of $\hat{\mathbf{z}}$ and Σ_{ts} is the covariance between $\hat{\mathbf{y}}$ and $\hat{\mathbf{z}}$. The joint Bayesian covariance matrix Π is defined similarly.

References

- [1] P. Hunt, S. Sarkar, *Reconstruction of the primordial power spectrum of curvature perturbations using multiple data sets*, JCAP **01** (2014) 025 [arXiv:1308.2317 [astro-ph.CO]].
- [2] P. A. R. Ade *et al.* [Planck Collaboration], *Planck 2013 results. XV. CMB power spectra and likelihood*, Astron. Astrophys. **571** (2014) A15 [arXiv:1303.5075 [astro-ph.CO]].
- [3] S. Das, *et al.* [ACT Collaboration], *The Atacama Cosmology Telescope: Temperature and Gravitational Lensing Power Spectrum Measurements from Three Seasons of Data*, JCAP **1404** (2014) 014 [arXiv:1301.1037 [astro-ph.CO]].
- [4] K. T. Story *et al.* [SPT Collaboration], *A measurement of the cosmic microwave background*

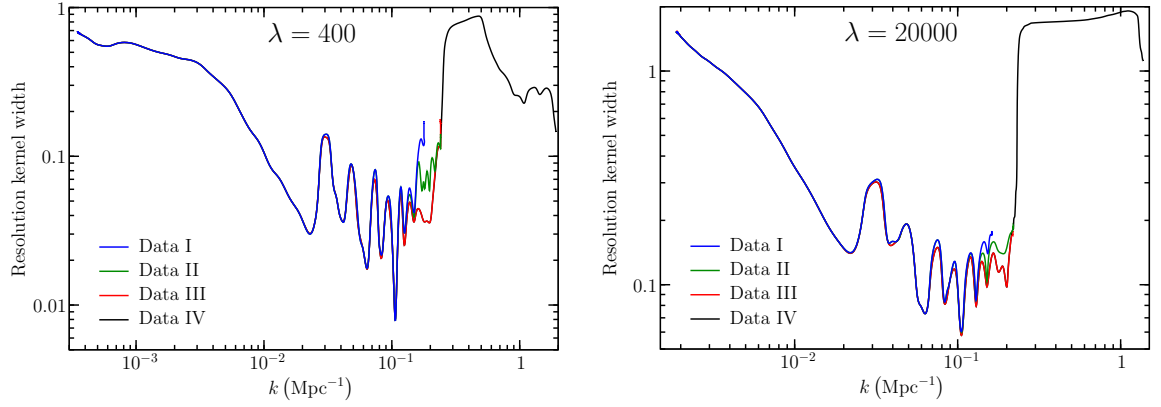


Figure 18. Left: resolution kernel width plotted against the kernel location with $\lambda = 400$ for the four data set combinations. Right: resolution kernel width plotted against the kernel location with $\lambda = 20000$ for the four data set combinations. The influence of the CMB acoustic peaks on the resolution is clearly apparent.

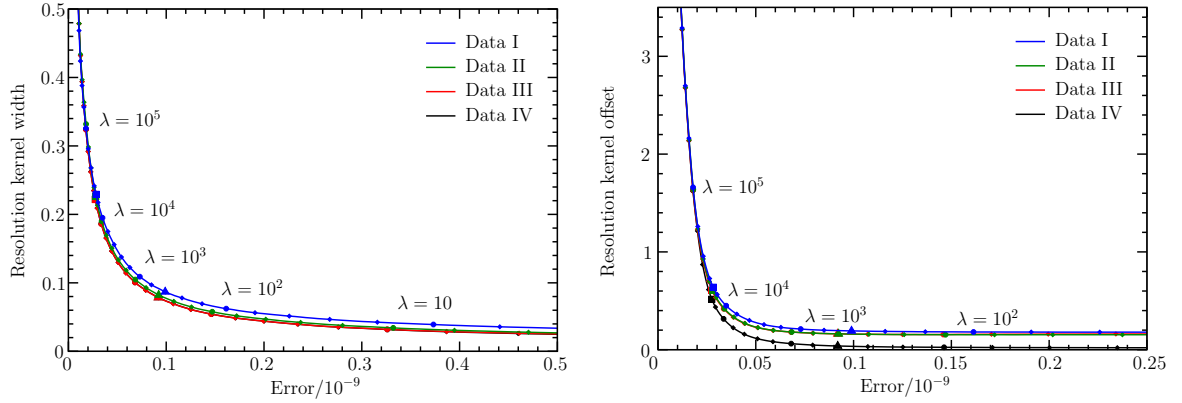


Figure 19. Left: trade-off curve of the resolution kernel width versus error as a function of the regularisation parameter λ for the four data set combinations. Right: trade-off curve of the resolution kernel offset versus error as a function of the regularisation parameter λ for the four data set combinations. In both panels the triangles and squares correspond to $\lambda = 400$ and $\lambda = 20000$ respectively, and the diamonds mark logarithmically equal intervals of λ .

damping tail from the 2500-square-degree SPT-SZ survey, *Astrophys. J.* **779** (2013) 86 [arXiv:1210.7231 [astro-ph.CO]].

- [5] P. A. R. Ade *et al.* [BICEP2 and Keck Array Collaborations], *BICEP2 / Keck Array V: Measurements of B-mode Polarization at Degree Angular Scales and 150 GHz by the Keck Array*, *Astrophys. J.* **811** (2015) 2, 126 [arXiv:1502.00643 [astro-ph.CO]].
- [6] D. Parkinson *et al.* [WiggleZ Collaboration], *The WiggleZ Dark Energy Survey: Final data release and cosmological results*, *Phys. Rev. D* **86** (2012) 103518. [arXiv:1210.2130 [astro-ph.CO]].
- [7] M. Kilbinger *et al.* [CFHTLenS Collaboration], *CFHTLenS: Combined probe cosmological model comparison using 2D weak gravitational lensing*, *Monthly Notices of the Royal Astronomical Society* **430** (2013) 3, 2200 [arXiv:1212.3338 [astro-ph.CO]].

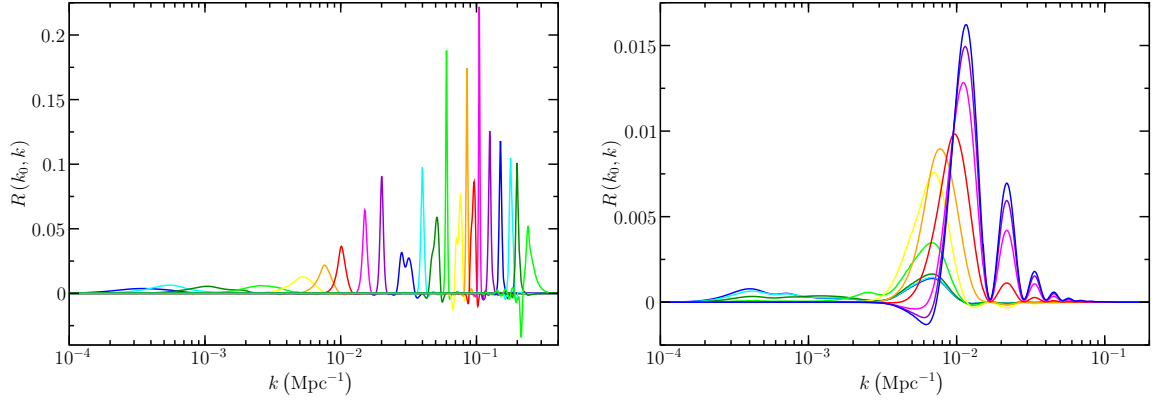


Figure 20. Left: the first-order scalar perturbation resolution kernels for the BICEP2/Keck Array, Planck, WMAP-9 polarisation, ACT, SPT, WiggleZ, galaxy clustering, CFTHLenS and Lyman- α data (combination V), in the presence of tensor perturbations, with $\lambda = 400$. The kernels are shown for $k_0 = 10^{-4}, 5 \times 10^{-4}, 10^{-3}, 2.5 \times 10^{-3}, 5 \times 10^{-3}, 7.5 \times 10^{-3}, 0.01, 0.015, 0.02, 0.03, 0.04, 0.05, 0.06, 0.075, 0.085, 0.095, 0.105, 0.125, 0.15, 0.18, 0.2 \text{ Mpc}^{-1}$. Right: the first-order tensor perturbation resolution kernels with $\lambda = 400$ for the same data sets in the presence of scalar perturbations. The kernels are shown for $k_0 = 10^{-4}, 5 \times 10^{-4}, 10^{-3}, 2.5 \times 10^{-3}, 5 \times 10^{-3}, 7.5 \times 10^{-3}, 0.01, 0.015, 0.02, 0.03 \text{ Mpc}^{-1}$.

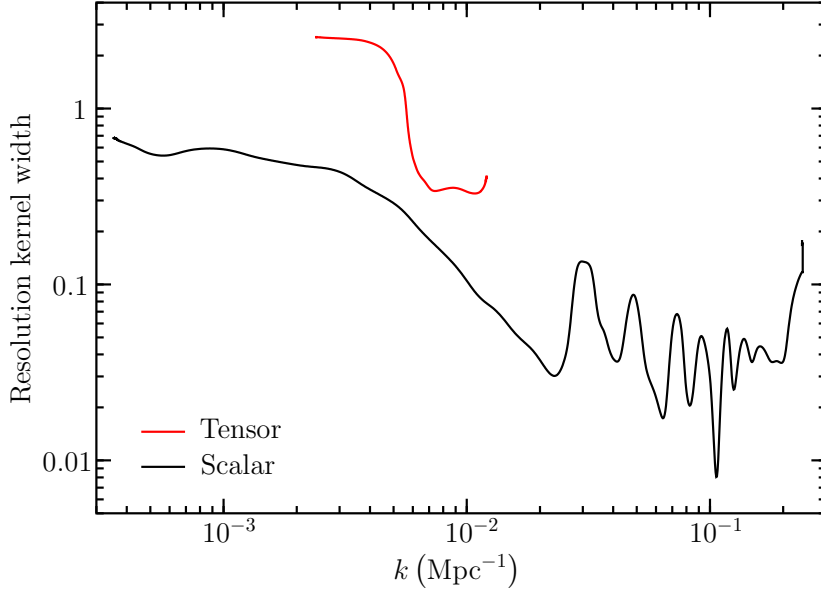


Figure 21. The scalar and tensor resolution kernel width plotted against kernel location with $\lambda = 400$ for the BICEP2/Keck Array, Planck, WMAP-9 polarisation, ACT, SPT, WiggleZ, galaxy clustering, CFTHLenS and Lyman- α data (combination V). The tensor reconstruction attains the greatest resolution at $k \simeq 0.01 \text{ Mpc}^{-1}$ driven by the BICEP2/Keck Array measurements.

- [8] M. Viel, M. G. Haehnelt and V. Springel, *Inferring the dark matter power spectrum from the Lyman-alpha forest in high-resolution QSO absorption spectra*, Mon. Not. Roy. Astron. Soc. **354** (2004) 684 [astro-ph/0404600].

- [9] P. A. R. Ade *et al.* [Planck Collaboration], *Planck 2013 results. XVI. Cosmological parameters*, Astron. Astrophys. **571** (2014) A16 [arXiv:1303.5076 [astro-ph.CO]].
- [10] D. K. Hazra, A. Shafieloo and G. F. Smoot, *Reconstruction of broad features in the primordial spectrum and inflaton potential from Planck*, JCAP **1312**, 035 (2013) [arXiv:1310.3038 [astro-ph.CO]].
- [11] G. Aslanyan, L. C. Price, K. N. Abazajian and R. Easther, *The Knotted Sky I: Planck constraints on the primordial power spectrum*, JCAP **1408** (2014) 052 [arXiv:1403.5849 [astro-ph.CO]].
- [12] P. A. R. Ade *et al.* [Planck Collaboration], *Planck 2015 results. XX. Constraints on inflation*, arXiv:1502.02114 [astro-ph.CO].
- [13] R. de Putter, E. V. Linder and A. Mishra, *Inflationary Freedom and Cosmological Neutrino Constraints*, Phys. Rev. D **89**, no. 10, 103502 (2014) [arXiv:1401.7022 [astro-ph.CO]].
- [14] S. Gariazzo, C. Giunti and M. Laveder, *Light Sterile Neutrinos and Inflationary Freedom*, JCAP **1504** (2015) 023 [arXiv:1412.7405 [astro-ph.CO]].
- [15] K. N. Abazajian, G. Aslanyan, R. Easther and L. C. Price, *The Knotted Sky II: Does BICEP2 require a nontrivial primordial power spectrum?*, JCAP **1408** (2014) 053 [arXiv:1403.5922 [astro-ph.CO]].
- [16] B. Hu, J. W. Hu, Z. K. Guo and R. G. Cai, *Reconstruction of the primordial power spectra with Planck and BICEP2 data*, Phys. Rev. D **90** (2014) 2, 023544 [arXiv:1404.3690 [astro-ph.CO]].
- [17] P. A. R. Ade *et al.* [Planck Collaboration], *Planck 2013 results. XXII. Constraints on inflation*, Astron. Astrophys. **571** (2014) A22 [arXiv:1303.5082 [astro-ph.CO]].
- [18] D. K. Hazra, A. Shafieloo and T. Souradeep, *Primordial power spectrum from Planck*, JCAP **1411** (2014) 11 [arXiv:1406.4827 [astro-ph.CO]].
- [19] P. Paykari, F. Lanusse, J. -L. Starck, F. Sureau and J. Bobin, *PRISM: Sparse Recovery of the Primordial Power Spectrum*, Astron. Astrophys. **566** (2014) A77 [arXiv:1402.1983 [astro-ph.CO]].
- [20] F. Lanusse, P. Paykari, J.-L. Starck, F. Sureau and J. Bobin, *PRISM: Recovery of the primordial spectrum from Planck data*, Astron. Astrophys. **571** (2014) L1 [arXiv:1410.2571 [astro-ph.CO]].
- [21] D. H. Lyth and A. R. Liddle, *The primordial density perturbation: Cosmology, inflation and the origin of structure*, Cambridge, UK: Cambridge Univ. Pr. (2009) 497 p
- [22] D. N. Spergel, R. Flauger and R. Hlozek, *Planck Data Reconsidered*, Phys. Rev. D **91** (2015) 2, 023518 [arXiv:1312.3313 [astro-ph.CO]].
- [23] J. Chluba, J. Hamann and S. P. Patil, *Features and New Physical Scales in Primordial Observables: Theory and Observation*, Int. J. Mod. Phys. D **24** (2015) 1530023 [arXiv:1505.01834 [astro-ph.CO]].
- [24] P. A. R. Ade *et al.* [BICEP2 Collaboration], *Detection of B-Mode Polarization at Degree Angular Scales by BICEP2*, Phys. Rev. Lett. **112** (2014) 24, 241101 [arXiv:1403.3985 [astro-ph.CO]].
- [25] S. Das *et al.*, *Detection of the Power Spectrum of Cosmic Microwave Background Lensing by the Atacama Cosmology Telescope*, Phys. Rev. Lett. **107** (2011) 021301 [arXiv:1103.2124 [astro-ph.CO]].
- [26] A. van Engelen *et al.*, *A measurement of gravitational lensing of the microwave background using South Pole Telescope data*, Astrophys. J. **756** (2012) 142 [arXiv:1202.0546 [astro-ph.CO]].
- [27] P. A. R. Ade *et al.* [Planck Collaboration], *Planck 2013 results. XVII. Gravitational lensing by large-scale structure*, Astron. Astrophys. **571**(2014) A17 [arXiv:1303.5077 [astro-ph.CO]].

- [28] A. Lewis and A. Challinor, *Weak gravitational lensing of the CMB*, Phys. Rept. **429** (2006) 1 [astro-ph/0601594].
- [29] A. Challinor and A. Lewis, *Lensed CMB power spectra from all-sky correlation functions*, Phys. Rev. D **71** (2005) 103010 [astro-ph/0502425].
- [30] U. Seljak, *Gravitational lensing effect on cosmic microwave background anisotropies: A Power spectrum approach*, Astrophys. J. **463** (1996) 1 [astro-ph/9505109].
- [31] M. Zaldarriaga and U. Seljak, *Gravitational lensing effect on cosmic microwave background polarization*, Phys. Rev. D **58** (1998) 023003 [astro-ph/9803150].
- [32] R. A. Battye and A. Moss, *Evidence for Massive Neutrinos from Cosmic Microwave Background and Lensing Observations*, Phys. Rev. Lett. **112** (2014) 5, 051303 [arXiv:1308.5870 [astro-ph.CO]].
- [33] N. MacCrann, J. Zuntz, S. Bridle, B. Jain and M. R. Becker, *Cosmic Discordance: Are Planck CMB and CFHTLenS weak lensing measurements out of tune?*, Mon. Not. Roy. Astron. Soc. **451** (2015) 2877 [arXiv:1408.4742 [astro-ph.CO]].
- [34] M. Raveri, *Is there concordance within the concordance Λ CDM model?*, arXiv:1510.00688 [astro-ph.CO].
- [35] P. A. R. Ade *et al.* [Planck Collaboration], *Planck 2015 results. XIII. Cosmological parameters*, arXiv:1502.01589 [astro-ph.CO].
- [36] J. W. Hu, R. G. Cai, Z. K. Guo and B. Hu, *Cosmological parameter estimation from CMB and X-ray cluster after Planck*, JCAP **1405** (2014) 020 [arXiv:1401.0717 [astro-ph.CO]].
- [37] L. Hoi and J. M. Cline, *Testing for Features in the Primordial Power Spectrum*, Int. J. Mod. Phys. D **18** (2009) 1863 [arXiv:0706.3887 [astro-ph]].
- [38] E. Gross and O. Vitells, *Trial factors or the look elsewhere effect in high energy physics*, Eur. Phys. J. C **70** (2010) 525 [arXiv:1005.1891 [physics.data-an]].
- [39] O. Vitells and E. Gross, *Estimating the significance of a signal in a multi-dimensional search*, Astropart. Phys. **35**, (2011) 230 [arXiv:1105.4355 [astro-ph.IM]].
- [40] M. Corts, A. R. Liddle and D. Parkinson, *Tensors, BICEP2 results, prior dependence, and dust*, Phys. Rev. D **92**, no. 6, 063511 (2015) [arXiv:1409.6530 [astro-ph.CO]].
- [41] C. L. Bennett *et al.* [WMAP Collaboration], *Nine-Year Wilkinson Microwave Anisotropy Probe (WMAP) Observations: Final Maps and Results*, Astrophys. J. Suppl. **208**, 20 (2013) [arXiv:1212.5225 [astro-ph.CO]].
- [42] D. K. Hazra, A. Shafieloo, G. F. Smoot and A. A. Starobinsky, *Ruling out the power-law form of the scalar primordial spectrum*, JCAP **1406**, 061 (2014) [arXiv:1403.7786 [astro-ph.CO]].
- [43] M. Gerbino, A. Marchini, L. Pagano, L. Salvati, E. Di Valentino and A. Melchiorri, *Blue gravity waves from BICEP2?*, Phys. Rev. D **90**, no. 4, 047301 (2014) [arXiv:1403.5732 [astro-ph.CO]].
- [44] Y. Wang and W. Xue, *Inflation and Alternatives with Blue Tensor Spectra*, JCAP **1410**, no. 10, 075 (2014) [arXiv:1403.5817 [astro-ph.CO]].
- [45] A. Ashoorioon, K. Dimopoulos, M. M. Sheikh-Jabbari and G. Shiu, *Non-BunchDavis initial state reconciles chaotic models with BICEP and Planck*, Phys. Lett. B **737**, 98 (2014) [arXiv:1403.6099 [hep-th]].
- [46] Y. F. Cai, J. O. Gong, S. Pi, E. N. Saridakis and S. Y. Wu, *On the possibility of blue tensor spectrum within single field inflation*, arXiv:1412.7241 [hep-th].
- [47] S. Mukohyama, R. Namba, M. Peloso and G. Shiu, *Blue Tensor Spectrum from Particle Production during Inflation*, JCAP **1408**, 036 (2014) [arXiv:1405.0346 [astro-ph.CO]].
- [48] Y. F. Cai and Y. Wang, *Testing quantum gravity effects with latest CMB observations*, Phys.

- Lett. B **735**, 108 (2014) [arXiv:1404.6672 [astro-ph.CO]].
- [49] R. H. Brandenberger, A. Nayeri and S. P. Patil, *Closed String Thermodynamics and a Blue Tensor Spectrum*, Phys. Rev. D **90**, no. 6, 067301 (2014) [arXiv:1403.4927 [astro-ph.CO]].
 - [50] T. Biswas, T. Koivisto and A. Mazumdar, *Atick-Witten Hagedorn Conjecture, near scale-invariant matter and blue-tilted gravity power spectrum*, JHEP **1408**, 116 (2014) [arXiv:1403.7163 [hep-th]].
 - [51] Y. F. Cai, J. Quintin, E. N. Saridakis and E. Wilson-Ewing, *Nonsingular bouncing cosmologies in light of BICEP2*, JCAP **1407**, 033 (2014) [arXiv:1404.4364 [astro-ph.CO]].
 - [52] <http://pla.esac.esa.int/pla/aio/planckResults.jsp?>
 - [53] P. A. R. Ade *et al.* [Planck Collaboration], *Planck 2013 results. VII. HFI time response and beams*, Astron. Astrophys. **571** (2014) A7 [arXiv:1303.5068 [astro-ph.IM]].
 - [54] P. A. R. Ade *et al.* [Planck Collaboration], *Planck 2013 results. VI. High Frequency Instrument data processing*, Astron. Astrophys. **571** (2014) A6 [arXiv:1303.5067 [astro-ph.CO]].
 - [55] J. Dunkley *et al.*, *The Atacama Cosmology Telescope: likelihood for small-scale CMB data*, JCAP **1307** (2013) 025 [arXiv:1301.0776 [astro-ph.CO]].
 - [56] C. L. Reichardt *et al.*, *A measurement of secondary cosmic microwave background anisotropies with two years of South Pole Telescope observations*, Astrophys. J. **755** (2012) 70. [arXiv:1111.0932 [astro-ph.CO]].
 - [57] R. E. Smith *et al.* [Virgo Consortium Collaboration], *Stable clustering, the halo model and nonlinear cosmological power spectra*, Mon. Not. Roy. Astron. Soc. **341** (2003) 1311 [astro-ph/0207664].
 - [58] R. A. C. Croft *et al.*, *Towards a precise measurement of matter clustering: Lyman alpha forest data at redshifts 2-4*, Astrophys. J. **581** (2002) 20 [astro-ph/0012324].
 - [59] T. S. Kim, M. Viel, M. G. Haehnelt, R. F. Carswell and S. Cristiani, *The power spectrum of the flux distribution in the lyman-alpha forest of a large sample of uves qso absorption spectra (luqas)*, Mon. Not. Roy. Astron. Soc. **347** (2004) 355 [astro-ph/0308103].
 - [60] N. Y. Gnedin and A. J. S. Hamilton, *Matter power spectrum from the Lyman-alpha forest: Myth or reality?*, Mon. Not. Roy. Astron. Soc. **334** (2002) 107 [astro-ph/0111194].
 - [61] J. Lesgourgues, M. Viel, M. G. Haehnelt and R. Massey, *A Combined analysis of Lyman-alpha forest, 3D Weak Lensing and WMAP year three data*, JCAP **0711** (2007) 008 [arXiv:0705.0533 [astro-ph]].
 - [62] A. Refregier, *Weak gravitational lensing by large scale structure*, Ann. Rev. Astron. Astrophys. **41** (2003) 645 [astro-ph/0307212].
 - [63] H. Hoekstra and B. Jain, *Weak Gravitational Lensing and its Cosmological Applications*, Ann. Rev. Nucl. Part. Sci. **58** (2008) 99 [arXiv:0805.0139 [astro-ph]].
 - [64] S. W. Allen, A. E. Evrard and A. B. Mantz, *Cosmological Parameters from Observations of Galaxy Clusters*, Ann. Rev. Astron. Astrophys. **49** (2011) 409 [arXiv:1103.4829 [astro-ph.CO]].
 - [65] D. H. Weinberg, M. J. Mortonson, D. J. Eisenstein, C. Hirata, A. G. Riess and E. Rozo, *Observational Probes of Cosmic Acceleration*, Phys. Rept. **530** (2013) 87 [arXiv:1201.2434 [astro-ph.CO]].
 - [66] P. A. R. Ade *et al.* [Planck Collaboration], *Planck 2013 results. XX. Cosmology from Sunyaev-Zeldovich cluster counts*, Astron. Astrophys. **571** (2014) A20 [arXiv:1303.5080 [astro-ph.CO]].
 - [67] A. Vikhlinin *et al.*, *Chandra Cluster Cosmology Project III: Cosmological Parameter Constraints*, Astrophys. J. **692** (2009) 1060

- [68] E. Rozo *et al.* [SDSS Collaboration], *Cosmological Constraints from the SDSS maxBCG Cluster Catalog*, *Astrophys. J.* **708** (2010) 645 [arXiv:0902.3702 [astro-ph.CO]].
- [69] M. Hasselfield *et al.*, *The Atacama Cosmology Telescope: Sunyaev-Zel'dovich selected galaxy clusters at 148 GHz from three seasons of data*, *JCAP* **1307** (2013) 008 [arXiv:1301.0816 [astro-ph.CO]].
- [70] H. Böhringer, G. Chon and C. A. Collins, *The extended ROSAT-ESO Flux Limited X-ray Galaxy Cluster Survey (REFLEX II) IV. X-ray Luminosity Function and First Constraints on Cosmological Parameters*, *Astron. Astrophys.* **570** (2014) A31 [arXiv:1403.2927 [astro-ph.CO]].
- [71] S. Bocquet *et al.*, *Mass Calibration and Cosmological Analysis of the SPT-SZ Galaxy Cluster Sample Using Velocity Dispersion σ_v and X-ray Y_X Measurements*, *Astrophys. J.* **799** (2015) 2, 214 [arXiv:1407.2942 [astro-ph.CO]].
- [72] K. M. Smith, C. Dvorkin, L. Boyle, N. Turok, M. Halpern, G. Hinshaw and B. Gold, *Quantifying the BICEP2-Planck Tension over Gravitational Waves*, *Phys. Rev. Lett.* **113**, no. 3, 031301 (2014) [arXiv:1404.0373 [astro-ph.CO]].
- [73] H. Liu, P. Mertsch and S. Sarkar, *Fingerprints of Galactic Loop I on the Cosmic Microwave Background*, *Astrophys. J.* **789** (2014) L29 [arXiv:1404.1899 [astro-ph.CO]].
- [74] M. J. Mortonson and U. Seljak, *A joint analysis of Planck and BICEP2 B modes including dust polarization uncertainty*, *JCAP* **1410** (2014) 10, 035 [arXiv:1405.5857 [astro-ph.CO]].
- [75] R. Flauger, J. C. Hill and D. N. Spergel, *Toward an Understanding of Foreground Emission in the BICEP2 Region*, *JCAP* **1408** (2014) 039 [arXiv:1405.7351 [astro-ph.CO]].
- [76] W. N. Colley and J. R. Gott, *Genus Topology and Cross-Correlation of BICEP2 and Planck 353 GHz B-Modes: Further Evidence Favoring Gravity Wave Detection*, *Mon. Not. Roy. Astron. Soc.* **447** (2015) 2034 [arXiv:1409.4491 [astro-ph.CO]].
- [77] R. Adam *et al.* [Planck Collaboration], *Planck intermediate results. XXX. The angular power spectrum of polarized dust emission at intermediate and high Galactic latitudes*, arXiv:1409.5738 [astro-ph.CO].
- [78] P. A. R. Ade *et al.* [BICEP2 and Planck Collaborations], *Joint Analysis of BICEP2/Keck Array and Planck Data*, *Phys. Rev. Lett.* **114** (2015) 101301 [arXiv:1502.00612 [astro-ph.CO]].
- [79] S. Hamimeche and A. Lewis, *Likelihood Analysis of CMB Temperature and Polarization Power Spectra*, *Phys. Rev. D* **77** (2008) 103013 [arXiv:0801.0554 [astro-ph]].
- [80] J. Hamann, J. Lesgourgues, G. Mangano, *Using BBN in cosmological parameter extraction from CMB: A Forecast for PLANCK*, *JCAP* **0803** (2008) 004 [arXiv:0712.2826].
- [81] J. A. Tauber *et al.* [Planck Collaboration], *Planck pre-launch status: the Planck mission*, *Astron. Astrophys.* **520** (2010) A2
- [82] M. R. Nolte *et al.* [WMAP collaboration], *Five-Year Wilkinson Microwave Anisotropy Probe (WMAP) observations: Angular power spectra*, *Astrophys. J. Suppl.* **180** (2009) 296 [arXiv:0803.0593].